Journal of
Mechanics of
Materials and Structures

HEXAGONAL BORON NITRIDE NANOSTRUCTURES:
A NANOSCALE MECHANICAL MODELING

Alessandra Genoese, Andrea Genoese and Ginevra Salerno

Volume 15, No. 2 March 2020

msp

JOURNAL OF MECHANICS OF MATERIALS AND STRUCTURES
Vol. 15, No. 2, 2020
dx.doi.org/10.2140/jomms.2020.15.249

HEXAGONAL BORON NITRIDE NANOSTRUCTURES: A NANOSCALE MECHANICAL MODELING

ALESSANDRA GENOESE, ANDREA GENOESE AND GINEVRA SALERNO

The paper deals with a numerical model for hexagonal boron nitride nanostructures. The model is developed in finite kinematics and takes into account binary, ternary and quaternary atomic interactions, described through the UFF potential with an *ad-hoc* set of parameters. Once validated with respect to *ab-initio* results of the tensile failure of boron nitride sheets under periodic conditions, the model is used to study the response of a sheet of finite size under traction, compression and shear.

1. Introduction

Over the last two decades, hexagonal nanostructures of carbon (C) atoms, such as graphene and carbon nanotubes, have received considerable attention for application in a variety of fields, including microelectronics, sensoring and actuation systems, energy storage, biotechnologies and composite materials [Nguyen and Nguyen 2016; Kumar et al. 2018; Mohan et al. 2018].

In addition to these nanostructures, attention has been also given to diatomic compounds, consisting, for instance, also of boron (B), nitrogen (N) and silicon (Si) atoms. Some examples are boron nitride (BN) and silicon carbide (SiC) nanosheets and the relative nanotubes. Similarly to their C analogues, these nanostructures exhibit exceptional thermal and mechanical properties, such as high thermal conductivity, low density, high tensile strength and membrane stiffness [Casady and Johnson 1996; Ouyang et al. 2010; Golberg et al. 2010]. Moreover, the different atomic composition leads to some specific properties, such as stronger resistance to oxidation and chemical stability at high temperatures, giving them advantages over C nanostructures in harsh environments [Casady and Johnson 1996; Golberg et al. 2010]. For this reason, these nanostructures have drawn attention in different technological fields, including the manufacture of semiconductors [Casady and Johnson 1996] (e.g., BN/graphene heterostructures for electronic devices) and hydrogen storage [Mpourmpakis et al. 2006]. In addition, BN compounds can also be cleaned and reused by means of heating and burning in air, are biocompatible, have low friction coefficient, have excellent sorption performance and are hydrorepellent. They are thus suitable for applications in medicine (e.g., drug delivery), as lubricants, for water filtration, for water purification from oil, solvents and dyes, as well as for the reinforcement or protection of composites [Golberg et al. 2010].

The understanding and control of the mechanical behavior of all these atomic nanostructures are key issues in the design of their composites and in many other contexts, such as nanosensors, nanoresonators, filtration, flexible nanoelectronics and so on [Shima 2012; Akinwande et al. 2017]. In this regard, it

Keywords: hexagonal boron nitride nanostructures, UFF potential, out-of-plane buckling.

is worth emphasizing also that the deformation influences the chemical-physical properties. Therefore, tuning these properties in specific applications through deformation control is possible, in principle.

All this has motivated a significant amount of experimental and theoretical works on the mechanics of these nanostructures [Krishnan et al. 1998; Kudin et al. 2001; Şahin et al. 2009; Wu et al. 2013; Vijayaraghavan and Zhang 2018; Sgouros et al. 2018; Jiang and Guo 2011; Le and Nguyen 2015; Genoese et al. 2017; 2018a; 2018b; 2019c; 2019a; 2019b; 2020; Favata et al. 2014; Davini et al. 2017; Korobeynikov et al. 2015, 2018, Giannopoulos et al. 2016; Tsiamaki et al. 2018; Tserpes and Vatistas 2015; Fazelzadeh and Ghavanloo 2014; Ghaffari et al. 2018; Hollerer 2014]. However, the technical difficulties and the costs of experiments make theoretical approaches preferable, for the time being.

In this regard, *ab-initio* simulations [Kudin et al. 2001; Şahin et al. 2009; Wu et al. 2013] are the most accurate tools to investigate the behaviors of atomic nanostructures. However, they demand a lot of computer power. For these reasons, in the mechanical field, they are generally used to characterize in very great detail the relaxed configuration of nanostructures (i.e., the self-equilibrated configuration) and their fundamental properties (e.g., the rigidities and the tensile strength) within standard continuum theories, solving problems with a limited number of atoms.

In view of the above, increasing attention has been given to molecular dynamics (MD) or molecular statics (MS) models [Vijayaraghavan and Zhang 2018; Sgouros et al. 2018; Jiang and Guo 2011; Le and Nguyen 2015; Genoese et al. 2017; 2018a; 2018b; 2019a; 2019b; 2019c; 2020; Favata et al. 2014; Davini et al. 2017; Korobeynikov et al. 2015, 2018] and their structural-mechanics approximations (e.g., beam or truss models of the atomic networks [Giannopoulos et al. 2016; Tsiamaki et al. 2018; Tserpes and Vatistas 2015]), as well as to continuum models [Fazelzadeh and Ghavanloo 2014; Ghaffari et al. 2018] and mixed models [Hollerer 2014], based on a multiscale representation of the matter.

Almost all the modeling works on the mechanics of diatomic nanostructures [Kudin et al. 2001; Şahin et al. 2009; Wu et al. 2013; Vijayaraghavan and Zhang 2018; Jiang and Guo 2011; Le and Nguyen 2015; Genoese et al. 2018a; 2019c; Giannopoulos et al. 2016; Tsiamaki et al. 2018] concern their linear behaviors only, in some cases [Genoese et al. 2018a; 2019c] using continuum mechanics to build a bridge between the *ab-initio* results and the MS model for a parameter refinement of simple interatomic potentials, such as the UFF one [Rappé et al. 1992].

In our opinion, MS models based on simple potentials are to be considered the best compromise between efficiency and accuracy at the atomic scale, above all in nonlinear contexts, where computational efficiency is a major requirement. However, for diatomic nanostructures nonlinear MS models are still lacking and there is also a few experience of the continuum and multiscale modeling. In relation to continuum modeling, if on one hand higher-order models, commonly used for periodic and hexagonal structures [Glaesener et al. 2019; Rizzi et al. 2019a; 2019b], are expected to be generally preferable [Auffray et al. 2015], on the other hand, quantitative comparisons between atomistic models and even simple continuum models are completely missing.

This paper deals with a numerical model of hexagonal BN nanostructures. An MS model that accounts for binary, ternary and quaternary atomic interactions is discussed, with reference to BN sheets. The model is developed in finite kinematics and the interactions are described through the UFF potential, endowed with an *ad-hoc* set of parameters. An assessment of the model and of its parameters is performed with respect to *ab-initio* results in terms of the tensile failure properties of a BN sheet, by considering periodic tensile tests in both the zigzag and the armchair directions. In addition, the nonlinear behavior

of a BN sheet of finite size is investigated in the case of traction, compression and shear in the zigzag and in the armchair directions, and in the case of pure shear. Space is also given to the discussion of the potential and to the choice of the parameters, as well as to some comparisons between the MS model and a thin shell model within buckling problems.

2. The MS model

The reference configuration of a diatomic sheet is assumed to be a planar monolayer of two different atom types, regularly alternating in the vertices of an hexagonal net so that all the atoms are bonded with an atom of the other type. Figure 1 (left) shows the configuration of a BN sheet. B and N atoms are represented with spheres of dimension proportional to the atomic radius, the atomic radius of N being smaller than that of B.

In MS models, one usually assumes that the reference configuration of the sheet is stress free and that the atoms are point-particles in Euclidean space. Their interactions are usually separated into two categories: bonding and long range. Long-range interactions are considered to be negligible with respect to the bonding ones. In turn, bonding interactions are usually distinguished between binary, ternary and quaternary interactions, measured in terms of the bond length[1] r_{ij}, valence angle ϑ_{ijk} and dihedral angle φ_{ijkl} (see Figure 1, right). In particular, the dihedral angle is the angle formed by two planes, the one identified by the positions of the atoms i, j and k and the other identified by the positions of the atoms i, j and l. In the literature [Rappé et al. 1992; Mayo et al. 1990; Blondel and Karplus 1996], the variations of the dihedral angle are also known as torsion of the central bond i-j of the four atoms i, j, k, l. The bonding interactions are derived from a potential U. Here, the UFF potential [Rappé et al. 1992] is adopted which is expressed in the additive form

$$U = \sum_b U_{ij} + \sum_a U_{ijk} + \sum_d U_{ijkl}, \tag{1}$$

where U_{ij}, U_{ijk} and U_{ijkl} are the energy contributions related to the b-th bond length, to the a-th valence angle and to the d-th dihedral angle, respectively. The energy contributions U_{ij}, U_{ijk} and U_{ijkl} are written

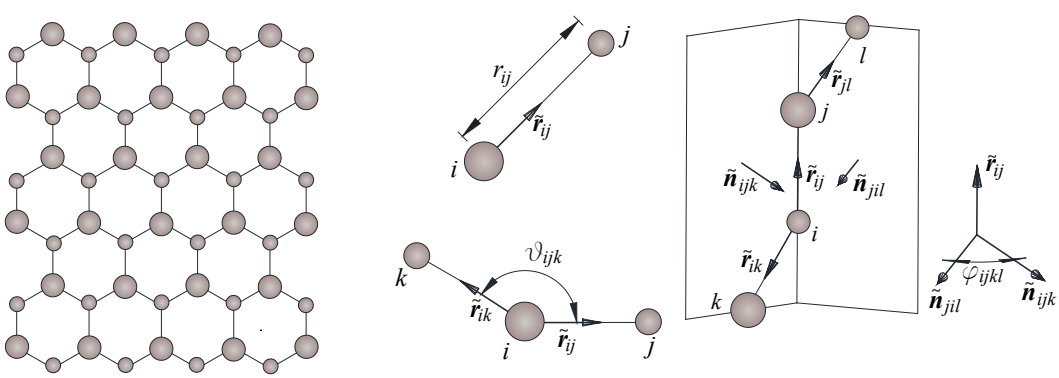

Figure 1. Atomistic model of the sheet: diatomic sheet (left) and atomistic kinematics (right).

[1] In atomistic models, the term bond is used to indicate a pair of two first nearest neighboring atoms.

using Morse and cosine functions, which are defined to be

$$U_{ij} = \overline{U}\left\{\left[1 - e^{-\beta(r_{ij}-\bar{r})}\right]^2 - 1\right\}, \tag{2a}$$

$$U_{ijk} = A\left(1 + 3\cos\vartheta_{ijk} - 4\cos^3\vartheta_{ijk}\right), \tag{2b}$$

$$U_{ijkl} = \frac{V}{2}\left\{1 - \cos\left[p\left(\varphi_{ijkl} - \bar{\varphi}_{ijkl}\right)\right]\right\}. \tag{2c}$$

In (2), $p = 2$, $\overline{U}$, β, A and V are parameters which we give later, while $\bar{r} \approx 0.145\,\text{nm}$ [Şahin et al. 2009] and $\bar{\varphi}_{ijkl} \in \{0, \pi\}$ are the bond length and the dihedral angle in the reference configuration of the sheet, where $\vartheta_{ijk} = \frac{2}{3}\pi$.

We denote by $\boldsymbol{x}_n$ and $\boldsymbol{r}_n$ the initial and the current position vectors of the n-th atom and by $\boldsymbol{u}_n = \boldsymbol{r}_n - \boldsymbol{x}_n$ its displacement vector. Then, $\boldsymbol{x}_{ij} = \boldsymbol{x}_j - \boldsymbol{x}_i$, $\boldsymbol{r}_{ij} = \boldsymbol{r}_j - \boldsymbol{r}_i$ and $\boldsymbol{u}_{ij} = \boldsymbol{u}_j - \boldsymbol{u}_i = \boldsymbol{r}_{ij} - \boldsymbol{x}_{ij}$ are the relative position vectors and the relative displacement vector of the atom j with respect to the atom i.

The bond length is given by

$$r_{ij} = \|\boldsymbol{r}_{ij}\| = \sqrt{\boldsymbol{r}_{ij} \cdot \boldsymbol{r}_{ij}}. \tag{3}$$

For what follows, $\tilde{\boldsymbol{r}}_{ij} = \boldsymbol{r}_{ij}/r_{ij}$ is the direction vector defined by a pair of atoms i-j. In addition, $\tilde{\boldsymbol{n}}_{ijk}$ and $\tilde{\boldsymbol{n}}_{jil}$ are, respectively, the unit vectors perpendicular to the plane determined by the current positions of the atoms i, j and k and to the plane determined by the current positions of the atoms j, l and i, given by

$$\begin{aligned} \tilde{\boldsymbol{n}}_{ijk} &= \frac{\boldsymbol{n}_{ijk}}{n_{ijk}}, \quad \boldsymbol{n}_{ijk} = \tilde{\boldsymbol{r}}_{ij} \times \tilde{\boldsymbol{r}}_{ik}, \quad n_{ijk} = \|\boldsymbol{n}_{ijk}\|, \\ \tilde{\boldsymbol{n}}_{jil} &= \frac{\boldsymbol{n}_{jil}}{n_{jil}}, \quad \boldsymbol{n}_{jil} = \tilde{\boldsymbol{r}}_{jl} \times \tilde{\boldsymbol{r}}_{ij}, \quad n_{jil} = \|\boldsymbol{n}_{jil}\|. \end{aligned} \tag{4}$$

The valence angle is defined as

$$\cos\vartheta_{ijk} = \tilde{\boldsymbol{r}}_{ij} \cdot \tilde{\boldsymbol{r}}_{ik}, \tag{5}$$

while the dihedral angle can be given in two different ways:

$$\cos\varphi_{ijkl} = \tilde{\boldsymbol{n}}_{ijk} \cdot \tilde{\boldsymbol{n}}_{jil}, \tag{6a}$$

$$\sin\varphi_{ijkl}\tilde{\boldsymbol{r}}_{ij} = \tilde{\boldsymbol{n}}_{jil} \times \tilde{\boldsymbol{n}}_{ijk}. \tag{6b}$$

At this point, we need to introduce the variations of r_{ij}, $\cos\vartheta_{ijk}$ and φ_{ijkl}. Starting from (3), we have

$$\delta r_{ij} = \tilde{\boldsymbol{r}}_{ij} \cdot \delta\boldsymbol{r}_{ij}, \tag{7}$$

$$\delta\tilde{\boldsymbol{r}}_{ij} = \frac{1}{r_{ij}}(\boldsymbol{I} - \tilde{\boldsymbol{r}}_{ij} \otimes \tilde{\boldsymbol{r}}_{ij})\,\delta\boldsymbol{r}_{ij}. \tag{8}$$

Similarly from (5) we obtain

$$\delta\cos\vartheta_{ijk} = \tilde{\boldsymbol{r}}_{ik} \cdot \delta\tilde{\boldsymbol{r}}_{ij} + \tilde{\boldsymbol{r}}_{ij} \cdot \delta\tilde{\boldsymbol{r}}_{ik}, \tag{9}$$

and by substituting (8) we have

$$\delta\cos\vartheta_{ijk} = \boldsymbol{n}_{ij}^{\vartheta} \cdot \delta\boldsymbol{r}_{ij} + \boldsymbol{n}_{ik}^{\vartheta} \cdot \delta\boldsymbol{r}_{ik}, \tag{10}$$

where

$$\boldsymbol{n}_{ij}^{\vartheta} = \frac{1}{r_{ij}}(\tilde{\boldsymbol{r}}_{ik} - \cos\vartheta_{ijk}\,\tilde{\boldsymbol{r}}_{ij}), \quad \boldsymbol{n}_{ik}^{\vartheta} = \frac{1}{r_{ik}}(\tilde{\boldsymbol{r}}_{ij} - \cos\vartheta_{ijk}\,\tilde{\boldsymbol{r}}_{ik}). \tag{11}$$

As for the variation of the dihedral angle $\delta\varphi_{ijkl}$, from (6a) we obtain

$$\delta\varphi_{ijkl} = \frac{d\varphi_{ijkl}}{d\cos\varphi_{ijkl}}\delta\cos\varphi_{ijkl} = -\frac{1}{\sin\varphi_{ijkl}}(\tilde{\boldsymbol{n}}_{jil}\cdot\delta\tilde{\boldsymbol{n}}_{ijk} + \tilde{\boldsymbol{n}}_{ijk}\cdot\delta\tilde{\boldsymbol{n}}_{jil}). \tag{12}$$

Performing for (12) the same calculations made for (9), we obtain

$$\delta\varphi_{ijkl} = -\frac{1}{\sin\varphi_{ijkl}}\left[\frac{1}{n_{ijk}}(\tilde{\boldsymbol{n}}_{jil} - \cos\varphi_{ijkl}\tilde{\boldsymbol{n}}_{ijk})\cdot\delta\boldsymbol{n}_{ijk} + \frac{1}{n_{jil}}(\tilde{\boldsymbol{n}}_{ijk} - \cos\varphi_{ijkl}\tilde{\boldsymbol{n}}_{jil})\cdot\delta\boldsymbol{n}_{jil}\right]. \tag{13}$$

Before proceeding, it is worth highlighting that the derivative $-1/\sin\varphi_{ijkl}$ is undetermined in the resting state where φ_{ijkl} is 0 or π. To eliminate this singularity, equation (13) is manipulated as in [Blondel and Karplus 1996] in order that the term $\sin\varphi_{ijkl}$ appears also in the numerator of the fraction, and thus can be deleted[2]. In particular, starting from (6), at first we obtain

$$\begin{aligned}
\sin\varphi_{ijkl}\,\tilde{\boldsymbol{n}}_{ijk}\times\tilde{\boldsymbol{r}}_{ij} &= \tilde{\boldsymbol{n}}_{ijk}\times(\tilde{\boldsymbol{n}}_{jil}\times\tilde{\boldsymbol{n}}_{ijk}) = \tilde{\boldsymbol{n}}_{jil} - \cos\varphi_{ijkl}\,\tilde{\boldsymbol{n}}_{ijk},\\
\sin\varphi_{ijkl}\,\tilde{\boldsymbol{n}}_{jil}\times\tilde{\boldsymbol{r}}_{ij} &= \tilde{\boldsymbol{n}}_{jil}\times(\tilde{\boldsymbol{n}}_{jil}\times\tilde{\boldsymbol{n}}_{ijk}) = \cos\varphi_{ijkl}\,\tilde{\boldsymbol{n}}_{jil} - \tilde{\boldsymbol{n}}_{ijk},
\end{aligned} \tag{14}$$

which, once substituted into (13), lead to

$$\delta\varphi_{ijkl} = -\frac{1}{n_{ijk}}\left(\tilde{\boldsymbol{n}}_{ijk}\times\tilde{\boldsymbol{r}}_{ij}\right)\cdot\delta\boldsymbol{n}_{ijk} + \frac{1}{n_{jil}}\left(\tilde{\boldsymbol{n}}_{jil}\times\tilde{\boldsymbol{r}}_{ij}\right)\cdot\delta\boldsymbol{n}_{jil}. \tag{15}$$

Using (4), equation (15) becomes

$$\delta\varphi_{ijkl} = \frac{1}{n_{ijk}^2}\left(\cos\vartheta_{ijk}\,\tilde{\boldsymbol{r}}_{ij} - \tilde{\boldsymbol{r}}_{ik}\right)\cdot\delta\boldsymbol{n}_{ijk} - \frac{1}{n_{jil}^2}\left(\cos\vartheta_{jil}\,\tilde{\boldsymbol{r}}_{ij} + \tilde{\boldsymbol{r}}_{jl}\right)\cdot\delta\boldsymbol{n}_{jil}, \tag{16}$$

where $\cos\vartheta_{ijk} = \tilde{\boldsymbol{r}}_{ij}\cdot\tilde{\boldsymbol{r}}_{ik}$ and $\cos\vartheta_{jil} = \tilde{\boldsymbol{r}}_{ji}\cdot\tilde{\boldsymbol{r}}_{jl} = -\tilde{\boldsymbol{r}}_{ij}\cdot\tilde{\boldsymbol{r}}_{jl}$.

Finally, after variation of (4) and further algebraic manipulations using the properties of the vector product, one obtains

$$\delta\varphi_{ijkl} = \boldsymbol{n}_{ij}^{\varphi}\cdot\delta\boldsymbol{r}_{ij} + \boldsymbol{n}_{ik}^{\varphi}\cdot\delta\boldsymbol{r}_{ik} + \boldsymbol{n}_{jl}^{\varphi}\cdot\delta\boldsymbol{r}_{jl}, \tag{17}$$

where we have set

$$\boldsymbol{n}_{ij}^{\varphi} = \frac{1}{r_{ij}}\left[\frac{\cos\vartheta_{jil}}{n_{jil}}\tilde{\boldsymbol{n}}_{jil} - \frac{\cos\vartheta_{ijk}}{n_{ijk}}\tilde{\boldsymbol{n}}_{ijk}\right], \quad \boldsymbol{n}_{ik}^{\varphi} = \frac{1}{r_{ik}\,n_{ijk}}\tilde{\boldsymbol{n}}_{ijk}, \quad \boldsymbol{n}_{jl}^{\varphi} = \frac{1}{r_{jl}\,n_{jil}}\tilde{\boldsymbol{n}}_{jil}. \tag{18}$$

[2]The kinematics will remain undetermined even when one length r_{ij} is zero. In addition, dihedral terms also become undetermined even when one of the norms (n_{jil} and n_{ijk}) is zero. However, these cases are highly unlikely to occur. Indeed, when $r_{ij} < \bar{r}$, a repulsive force arises between the atoms i and j, whose value exponentially increases as r_{ij} tends to zero. This is obviously a strong impediment to further decreasing the distance between the two atoms. Moreover, having $n_{ijk} = \sin\vartheta_{ijk}$ or $n_{jil} = \sin\vartheta_{jil}$ equal to zero would imply that $\tilde{\boldsymbol{r}}_{ij}$ is colinear to $\tilde{\boldsymbol{r}}_{ik}$ or $\tilde{\boldsymbol{r}}_{ij}$ is colinear to $\tilde{\boldsymbol{r}}_{jl}$, but also this situation is improbable, because ternary interactions prevent the atoms i, j, k and j, i, l from being aligned.

The equilibrium configurations of the system are sought through the stationarity condition of its total potential energy

$$\Pi = U - \sum_n \boldsymbol{p}_n \cdot \boldsymbol{u}_n, \tag{19}$$

where U, defined in (1) and (2), is a function of the displacements and $\boldsymbol{p}_n$ is the force applied to the n-th atom. Recalling (7), (10) and (17), the variation of the potential U is

$$\delta U = \sum_b \delta \boldsymbol{r}_{ij} \cdot \boldsymbol{s}^r_{ij} + \sum_a \left(\delta \boldsymbol{r}_{ij} \cdot \boldsymbol{s}^\vartheta_{ij} + \delta \boldsymbol{r}_{ik} \cdot \boldsymbol{s}^\vartheta_{ik}\right) + \sum_d \left(\delta \boldsymbol{r}_{ij} \cdot \boldsymbol{s}^\varphi_{ij} + \delta \boldsymbol{r}_{ik} \cdot \boldsymbol{s}^\varphi_{ik} + \delta \boldsymbol{r}_{jl} \cdot \boldsymbol{s}^\varphi_{jl}\right), \tag{20}$$

where

$$\boldsymbol{s}^r_{ij} = \frac{dU_{ij}}{dr_{ij}} \tilde{\boldsymbol{r}}_{ij}, \tag{21a}$$

$$\boldsymbol{s}^\vartheta_\alpha = \frac{dU^\vartheta_{ijk}}{d\cos\vartheta_{ijk}} \boldsymbol{n}^\vartheta_\alpha, \quad \alpha \in \{ij,\ ik\}, \tag{21b}$$

$$\boldsymbol{s}^\varphi_\beta = \frac{dU^\varphi_{ijkl}}{d\varphi_{ijkl}} \boldsymbol{n}^\varphi_\beta, \quad \beta \in \{ij,\ ik,\ jl\}, \tag{21c}$$

are the force vectors related to the binary, ternary and quaternary interactions.

The derivatives of the potential functions are given in Appendix A. Finally, the equilibrium equations assume the following form

$$\sum_b \boldsymbol{s}^r_{ij} \cdot (\delta \boldsymbol{r}_j - \delta \boldsymbol{r}_i) + \sum_a \left[\boldsymbol{s}^\vartheta_{ij} \cdot (\delta \boldsymbol{r}_j - \delta \boldsymbol{r}_i) + \boldsymbol{s}^\vartheta_{ik} \cdot (\delta \boldsymbol{r}_k - \delta \boldsymbol{r}_i)\right] + \sum_d \left[\boldsymbol{s}^\varphi_{ij} \cdot (\delta \boldsymbol{r}_j - \delta \boldsymbol{r}_i) + \boldsymbol{s}^\varphi_{ik} \cdot (\delta \boldsymbol{r}_k - \delta \boldsymbol{r}_i) + \boldsymbol{s}^\varphi_{jl} \cdot (\delta \boldsymbol{r}_l - \delta \boldsymbol{r}_j)\right] = \sum_n \boldsymbol{p}_n \cdot \delta \boldsymbol{r}_n, \tag{22}$$

for any admissible $\delta \boldsymbol{r}_n$.

The MS model, described so far, has been implemented in a custom-made MATLAB computer code. The equilibrium equations are solved through the arc-length method. More details about it are given in [Riks 1979; Garcea et al. 1998], while the second variation of the potential, which implicitly defines the tangent operator, is reported in Appendix B.

3. The parameters of the potential

The potential functions given in (2) are characterized by four parameters $\overline{U}$, β, A and V. Following [Rappé et al. 1992], we characterize the diatomic net by a unique value for $\overline{U}$, β and V, since all the bonds involve one N atom and one B atom and behave in the same way versus the length variations and the torsions. Instead, two different values of A are required, i.e., A_B and A_N, depending on whether the bonds i-j and i-k share the B atom or the N atom.

The choice of these parameters is carried out through a constitutive identification procedure which uses *ab-initio* solutions, found in the literature, as reference values of some mechanical properties of BN sheets. In particular, the full decoupling of the potential functions with respect to the deformation parameters allow us to separate the determination of $\overline{U}$, β, A_B and A_N from that of V in two different

moments, in which the sheet is respectively seen as a linear Cauchy membrane and as a linear Kirchhoff plate.

From a methodological point of view, we first determine the values of the three force constants k^r, k^ϑ and k^φ, as

$$k^r = \frac{d^2U_{ij}}{dr_{ij}^2}\bigg|_{r_{ij}=\bar{r}} = 2\bar{U}\beta^2, \quad k^\vartheta = \frac{d^2U_{ijk}}{d\vartheta_{ijk}^2}\bigg|_{\vartheta_{ijk}=\bar{\vartheta}} = 9A, \quad k^\varphi = \frac{d^2U_{ijhk}}{d\varphi_{ijkl}^2}\bigg|_{\varphi_{ijkl}=\bar{\varphi}_{ijkl}} = 2V, \tag{23}$$

and later the values of parameters β, A and V of the potential, once fixed $\bar{U}$. This choice is justified by the fact that the force constants are framed within the UFF model [Rappé et al. 1992] and well known in the literature as the only constitutive ingredients of harmonic potentials. Obviously, given that we have chosen to differentiate the values of A into A_B and A_N, the force constant k^ϑ will take on two distinct values, k_B^ϑ and k_N^ϑ, through (23).

As for the determination of k^r, k_B^ϑ and k_N^ϑ, in [Genoese et al. 2018a] we derived, through an exact continualization procedure of the sheet as a linear membrane, the following

$$Y = \frac{4\sqrt{3}\,k^r(k_B^\vartheta + k_N^\vartheta)}{k^r\bar{r}^2 + 9(k_B^\vartheta + k_N^\vartheta)}, \qquad \nu = \frac{k^r\bar{r}^2 - 3(k_B^\vartheta + k_N^\vartheta)}{k^r\bar{r}^2 + 9(k_B^\vartheta + k_N^\vartheta)}, \tag{24}$$

which directly link the 2D Young modulus Y and the Poisson coefficient ν, to the aforementioned constants and to the nanoscale geometry. In the same work [Genoese et al. 2018a], making use of the UFF hypothesis [Rappé et al. 1992], which links the force constants k_B^ϑ and k_N^ϑ to the effective charges Z_B and Z_N of B and N atoms as

$$k_B^\vartheta / k_N^\vartheta = Z_N^2 / Z_B^2 \approx 2.10, \tag{25}$$

we obtained $k^r = 585\,\text{nN/nm}$, $k_B^\vartheta = 1.347\,\text{aJ}$ and $k_N^\vartheta = 0.641\,\text{aJ}$ from the *ab-initio* results $Y = 267\,\text{nN/nm}$ and $\nu = 0.21$, given in [Şahin et al. 2009]. Adding to these three values the *ab-initio* result $\bar{U} = 0.64\,\text{aJ}$, given in [Nozaki and Itoh 1996], we obtained through (23): $\beta = 21.38\,\text{nm}^{-1}$, $A_B = 0.1497\,\text{aJ}$ and $A_N = 0.0712\,\text{aJ}$, further validated in [Genoese et al. 2019c] in a different context.

As regards the determination of k^φ, this is carried out here, by modeling the sheet as a linear Kirchhoff plate, equating the expression of bending rigidity, in terms of the nanoscopic geometry and of k^φ, to its *ab-initio* counterpart, given in [Kudin et al. 2001]. The continualization of the sheet is done through a variational procedure, already used in similar contexts of periodic discrete systems [Genoese et al. 2017; 2018a; 2018b; Salerno and de Felice 2009]. In particular, we first select a reference elementary volume (REV), then we establish a map between continuous and atomistic kinematics, and finally we assume the bending strain energy density of the plate and the dihedral energy density of the nanoscopic model to coincide.

In Figure 2 the REV is shown together with its extension, and a Cartesian frame (O, x, y, z) is given. The proper REV is the dashed lozenge, which contains atoms number 7 and 8, but to these must be added all the atoms, numbered in figure, that define the dihedral angles related to the torsion of the five bonds, 7-8, 7-4, 7-10, 8-5 and 8-11.

On the extended REV the following displacement field is imposed:

$$\boldsymbol{u}(x, y) = -\tfrac{1}{2}\big(\chi_x\, x^2 + \chi_y\, y^2 + \chi_{xy}\, xy\big)\boldsymbol{e}_z, \tag{26}$$

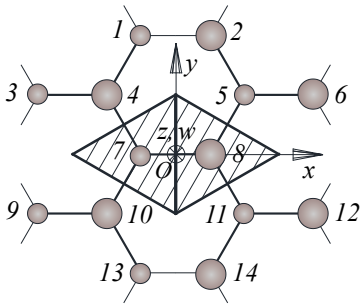

Figure 2. The REV and its extension.

which is induced by uniform bending χ_x, χ_y and twisting χ_{xy} curvatures, $\boldsymbol{e}_z$ being the unit vector perpendicular to the plane.

Then, following Cauchy–Born rule[3], the i-th atom of the extended REV is constrained to displace according to (26)

$$\boldsymbol{u}_i = -\tfrac{1}{2}\big(\chi_x\, x_i^2 + \chi_y\, y_i^2 + \chi_{xy}\, x_i\, y_i\big)\boldsymbol{e}_z. \tag{27}$$

Now, the dihedral energy density is given by

$$\Phi = \frac{1}{\mathscr{A}} \sum_d U_{ijkl}\, \mathscr{W}_{ijkl}, \tag{28}$$

where summation extends to all the aforementioned dihedral contributions, $\mathscr{A}$ is the REV area and $\mathscr{W}_{ijkl}$ measure the effective fraction of the bonds within the REV.

Within the linearized context, the potential U_{ijkl} defined in (2c) assumes the following quadratic form

$$U_{ijkl} = \frac{k^\varphi}{2} \Delta\varphi_{ijkl}^2, \tag{29}$$

where, through (17), $\Delta\varphi_{ijkl}$ is given by

$$\Delta\varphi_{ijkl} = \boldsymbol{n}_{ij}^\varphi \cdot \boldsymbol{u}_{ij} + \boldsymbol{n}_{ik}^\varphi \cdot \boldsymbol{u}_{ik} + \boldsymbol{n}_{jl}^\varphi \cdot \boldsymbol{u}_{jl}, \tag{30}$$

$\boldsymbol{n}_{ij}^\varphi$, $\boldsymbol{n}_{ik}^\varphi$ and $\boldsymbol{n}_{jl}^\varphi$ being evaluated in the planar configuration of the sheet and $\boldsymbol{u}_{ij}$, $\boldsymbol{u}_{ik}$ and $\boldsymbol{u}_{jl}$ determined through (27).

By substituting (29) and (30) into (28), the energy density Φ turns out to be a quadratic function of the curvatures and the elastic rigidities of the plate are easily obtained to be

$$\begin{aligned} D_{11} &= \frac{\partial^2\Phi}{\partial\chi_x^2} = \frac{7\sqrt{3}}{3}k^\varphi, \qquad D_{22} = \frac{\partial^2\Phi}{\partial\chi_y^2} = \frac{7\sqrt{3}}{3}k^\varphi, \\ D_{12} &= \frac{\partial^2\Phi}{\partial\chi_x\partial\chi_y} = -\frac{\sqrt{3}}{3}k^\varphi, \quad D_{33} = \frac{\partial^2\Phi}{\partial\chi_{xy}^2} = \frac{4\sqrt{3}}{3}k^\varphi, \end{aligned} \tag{31}$$

[3]Cauchy–Born rule generally induces equilibrium errors in the identification procedure. In this case, however, it can be shown that the kinematic map chosen corresponds also to an equilibrated state for the atomistic system.

while

$$\frac{\partial^2 \Phi}{\partial \chi_x \chi_{xy}} = \frac{\partial^2 \Phi}{\partial \chi_y \chi_{xy}} = 0.$$

Finally, by exploiting the result $D_{11} = D_{22} = D$ and the *ab-initio* reference $D = 0.2067$ nN nm, given in [Kudin et al. 2001], one obtains $k^{\varphi} = 0.052$ aJ and then, from (23), $V = 0.026$ aJ.

To complete this section, we consider it interesting to make some considerations on the three-dimensional material identified. If we rewrite the plate rigidities in terms of the 2D Young and shear moduli, Y and $\widetilde{G}$, the Poisson ratio ν and the thickness t, that is,

$$D_{11} = \frac{Yt^2}{12(1-\nu^2)}, \quad D_{12} = \nu\frac{Yt^2}{12(1-\nu^2)}, \quad D_{33} = \frac{\widetilde{G}t^2}{12}. \tag{32}$$

From (31) we obtain

$$\nu = D_{12}/D_{11} = -\tfrac{1}{7}$$

which is different from $\nu = 0.21$, obtained as *ab-initio* result for the membrane. This result, also found for graphene in other works in literature [Davini et al. 2017], can be interpreted as the impossibility of modeling monoatomic and diatomic sheets as one 3D Cauchy isotropic material. However, making use of the first and third equations of (32) with the first and fourth equations of (31), one obtains

$$\widetilde{G}t^2 = 16\sqrt{3}\,k^{\varphi} = \frac{Yt^2}{2(1+\nu)}, \tag{33}$$

making use of $\nu = -\frac{1}{7}$. Equation (33) is an isotropic relationship, albeit with a Poisson coefficient different from that obtained from plane problems. This can be interpreted as the confirmation that standard continuum models, while giving two different materials for the in-plane and the out-of-plane behaviors of the sheet, nevertheless interpret the hexagonal symmetry as isotropy.

4. Periodic tests

In this section, we propose an assessment of the model with respect to the *ab-initio* results in terms of the tensile failure properties of a sheet, by performing periodic tensile tests in both the zigzag and the armchair directions (zigzag and armchair tensile tests, respectively). We consider an hexagonal ring with the outermost elements cut, through the addition of fictitious nodes, as shown in Figure 3 to ensure periodic variations of the valence angles. These elements are loaded with the point forces defined (see Figure 3), Q being a tensile load for unit length.

For the outermost elements, the two body potential U_{ij} is modified in order to obtain the same forces as in the corresponding inner elements and to correct the rigidities according to the lengths. We consider the following expression

$$U_{ij} = \alpha_{ij}\overline{U}\left\{\left[1 - e^{-\beta(r_{ij}/\alpha_{ij} - \bar{r})}\right]^2 - 1\right\}, \tag{34}$$

where α_{ij} is equal to α_B or to α_N, both defined in the Figure 3. In particular, α_{ij} is equal to α_B for the outermost elements having the B atom, while α_{ij} is equal to α_N for the outermost elements having the N atom.

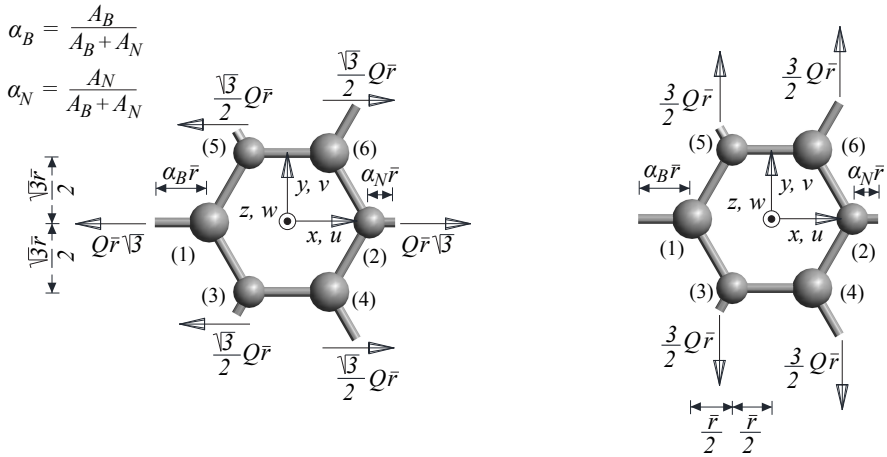

Figure 3. Applied forces under periodic boundary conditions: zigzag test (left) and armchair test (right).

In the numerical tests, the in-plane rigid body motions are filtered by imposing a symmetry condition with respect to the x-axis and zeroing the average of the x-displacements. In more detail, letting u_i and v_i be the x-displacement and the y-displacement of the i-th atom, we impose $v_1 = v_2 = 0$ and $\sum_{i=1}^{6} u_i = 0$.

To compare with the *ab-initio* results, the equilibrium paths are represented, for both tests, in terms of the engineering stresses and strains, which substantially correspond to those of a first order problem, although our model is fully nonlinear.

For each equilibrium point, the stress is directly Q, while the strain is $\varepsilon = (u_2 - u_1)/2\bar{r}$ in the zigzag tensile test and $\varepsilon = (v_5 + v_6)/2\bar{r}\sqrt{3} - (v_3 + v_4)/2\bar{r}\sqrt{3}$ in the armchair tensile test. As already found for graphene [Genoese et al. 2019b], the equilibrium paths, shown in Figure 4 (left), are characterized by a limit point, followed by a softening branch. From a qualitative point of view, they follow the same trend as the inner forces related to the binary energy terms, the expression of which is obtainable by differentiation of (2a). This behavior can be explained considering that the deformation of the sheet essentially consists in the elongation of the bonds and the crisis is driven by the most stretched ones, which are those parallel to the load direction or close to the load direction, as we can deduce from the configurations in Figure 4 (right). For this precise reason, the sheet shows a limit value of Q in the armchair direction about 22% greater than that in the zigzag direction (see Figure 4, left), i.e., the sheet is stronger along the armchair direction than in the zigzag one.

In addition, the values of ε in the armchair direction are greater than those in the zigzag direction by about 34% at the limit configuration, depicted in Figure 4 (right top), and along the softening branch. The difference in the limit values depends on the different inclination of the most stretched bonds with respect to the external load direction: since in the armchair test these bonds are inclined with respect to the load direction, they reach their crisis condition at higher loads than in the zigzag test, where the stretched bonds are parallel to the load. In both cases the failure modes are brittle with a rapid decrease in stress after the failure peak.

However, along the softening branch, considerable elongations of the bonds are achieved. They correspond to unrealistic interatomic distances, at which it is hard to believe that the first neighbouring atoms

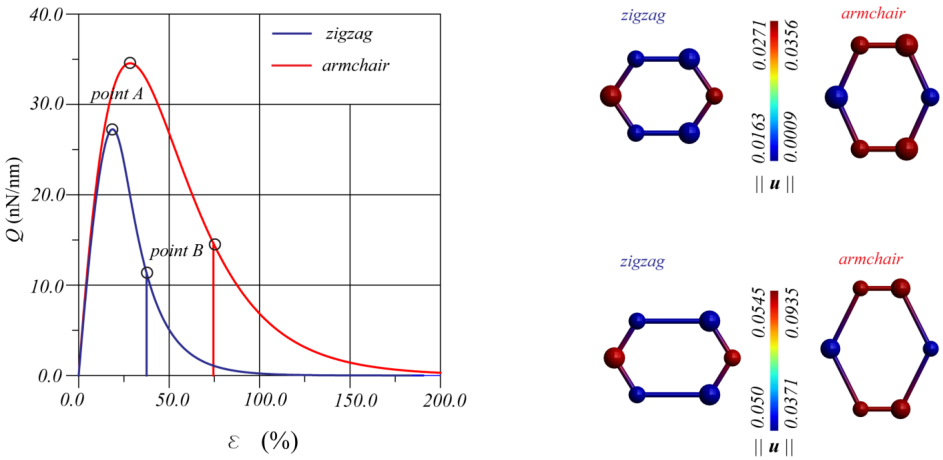

Figure 4. Zigzag and armchair tensile tests under periodic boundary conditions: equilibrium paths (left), deformed configurations at point A (right top) and deformed configurations at point B (right bottom).

direction		present study	[Wu et al. 2013]
zigzag	ε	0.187	0.18
	Q	27.2	29.0
armchair	ε	0.283	0.29
	Q	34.6	33.7

Table 1. Limit values of strain and 2D stress (nN/nm) compared with the literature.

still interact with each other. For this reason, a cutoff bond length is generally introduced, so defining a bond-breaking criterion. In this work, we choose a reasonable cutoff bond length of 0.245 nm. The vertical lines drawn in Figure 4 (left) correspond to the cutoff configurations depicted in the Figure 4 (right bottom).

In Table 1, our limit values of both the engineering strains and stresses are compared with the *ab-initio* results in [Wu et al. 2013]. Percentage differences of about 3% are registered in the zigzag test, while percentage differences of about 4% and 6% are registered in the armchair test for strain and stress, respectively. Analysis of the results shows a good agreement with the reference values and this can be considered as a further assessment of the potential parameters which we exploit.

5. Tensile, compression and shear tests on a BN sheet of finite size

In this section, tensile, compression and shear tests on a BN sheet of finite size are addressed. The tensile tests are performed in order to emphasize bifurcation phenomena already found in the case of graphene [Genoese et al. 2019b], while compression and shear tests are performed in order to study out-of-plane buckling behaviors. The selected sheet presents an almost square shape, with length $a = 10.508$ nm and width $b = 10.084$ nm, and consists of 4150 atoms.

5.1. ***Tensile tests.*** Figure 5 shows the geometry of the sheet and the point forces applied in the tensile tests, Q being again the load for unit length. Similarly to the periodic case, the in-plane rigid body motions are filtered by imposing $v_i = 0$ on the central horizontal row of the atoms and $\sum_{i=1}^{n_a} u_i = 0$, where n_a is the total number of atoms of the sheet.

The equilibrium paths are given until the cutoff bond length is reached. In this case, the engineering strains ε are evaluated on the basis of average values of the displacements of the sides. In particular, for the zigzag test and for the armchair test, respectively, strains are evaluated as $\varepsilon = \Delta u/a = (\bar{u}_4 - \bar{u}_3)/a$ and $\varepsilon = \Delta v/b = (\bar{v}_2 - \bar{v}_1)/b$, where $\bar{u}_k$ and $\bar{v}_k$ are the mean values of the displacements along x and y on the side k.

Figure 6 (top left) shows the equilibrium paths of the BN sheet of finite size and the precritical paths under periodic conditions (see Section 3). The equilibrium paths of the BN sheet of finite size present a bifurcation point before the corresponding limit point under periodic conditions, and a return back of the bifurcated paths nearly superimposable to the precritical paths, as already observed in the case of graphene sheets of finite size [Genoese et al. 2019b].

This trend of the paths can be explained as a phenomenon of localization of the deformation only in some bonds, which are the first to reach the crisis, i.e., the maximum inner force, and which finally break, reaching the cutoff length. Both the bifurcation (point A) and the cutoff (point B) configurations are shown in Figure 6 (top right) and Figure 6 (bottom), respectively; the latter shows the details of the bonds where the deformation is localized up to the point where it breaks. The return of the paths depends on the fact that, during the evolution of process, these bonds continue to be stretched by an even smaller force, while all the other bonds relax, i.e., all bonds experience a net decrease of their inner force. In

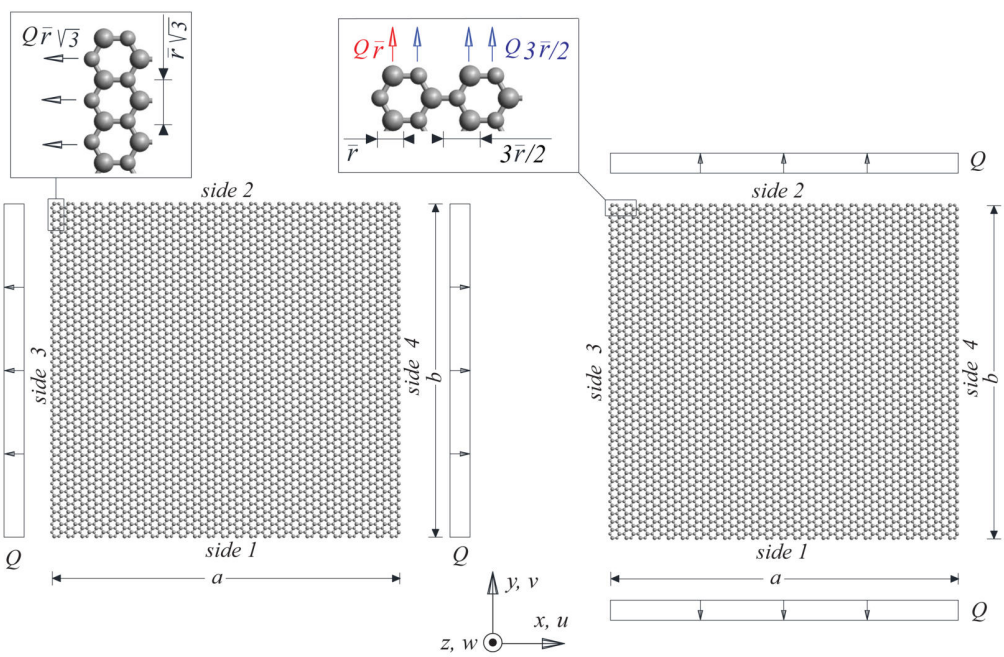

Figure 5. BN sheet under tensile loads in the zigzag (left) and armchair (right) directions.

addition, while only very few bonds reach the cutoff length, all the others become shorter; this produces an average shortening of the sheet in the postcritical paths.

Differently to the case of graphene, localization and then the break of the bonds involves only the portions on the right of the sheet, near the edges, as reported in detail in Figure 6 (bottom). This happens because of the presence of two types of atoms in the hexagonal rings.

Localization phenomena give rise to a reduction of the tensile failure properties, as it is clear from Table 2, where the bifurcation values of the strains and stresses are compared with their limit counterpart under periodic boundary conditions. In particular, localization phenomena are more penalising when the tensile load is applied in the armchair direction with a reduction of 9% for the stress and 35% for the strain.

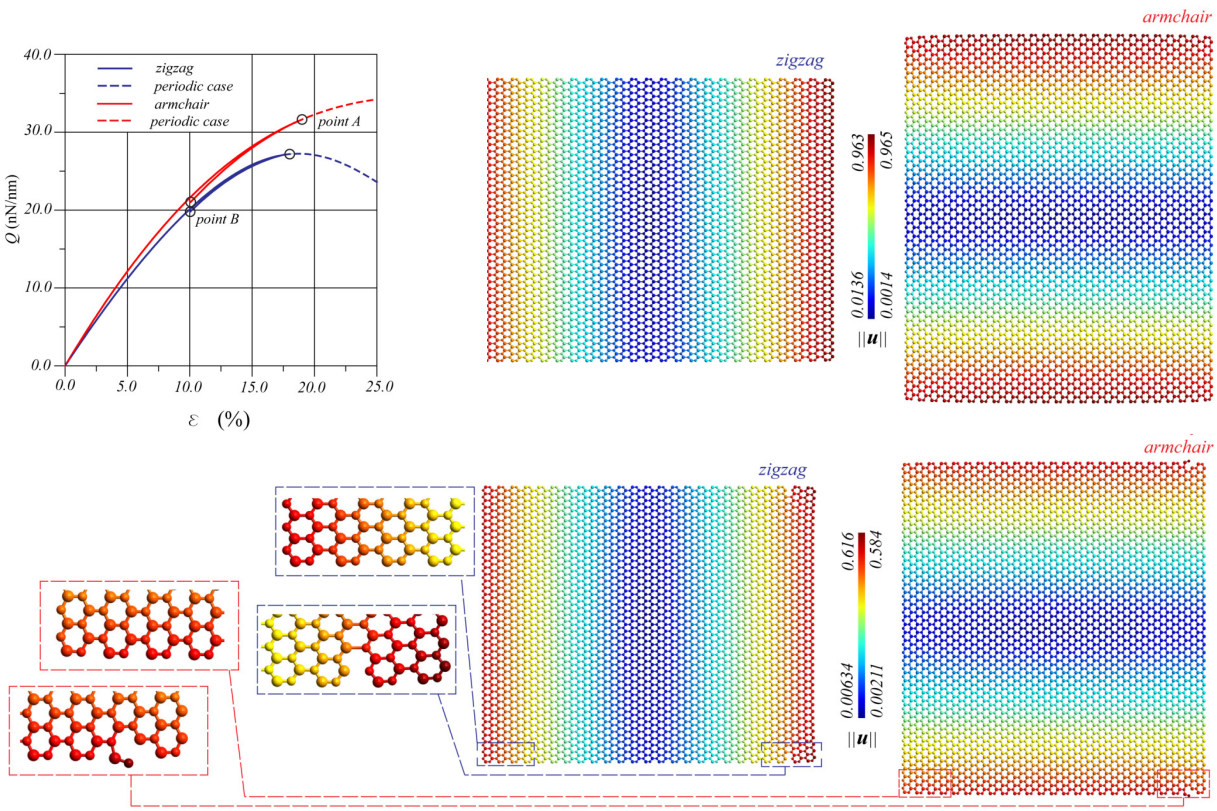

Figure 6. Equilibrium paths (top left) and deformed configurations at point A (top right) and point B (bottom).

direction	bifurcation values ε	bifurcation values Q	limit values ε	limit values Q
zigzag	0.177	26.9	0.187	27.2
armchair	0.184	31.5	0.283	34.6

Table 2. Bifurcation values versus limit values of the engineering strains and stresses (nN/nm).

5.2. ***Compression tests.*** The BN sheet of finite size is now studied under compression loads in the zigzag direction and in the armchair direction, as shown in Figure 7. Two different constraint conditions on the out-of-plane displacements are considered, namely conditions of simple support only on the loaded sides and conditions of simple support on all the sides. In both cases, the in-plane rigid body motions are filtered as in the tensile tests. In addition, small imperfection forces, equal to each other, are applied to the atoms marked in red, perpendicularly to the plane of the sheet.

Comparisons are also performed with an isotropic thin shell, with linear elastic constitutive relationship, identified from the *ab-initio* results $Y = Et = 267\,\text{nN/nm}$, $\nu = 0.21$ and $D = Et^3/12(1-\nu^2) = 0.2067\,\text{nN nm}$, where E is the Young modulus and t is obtained from the bending stiffness value. The choice of this continuum stems from the fact that this is the model to which *ab-initio* solutions refer and that we have used to calibrate the interatomic potential. Therefore, the following figures show both the equilibrium paths provided by the MS model and by the nonlinear analysis provided by ABAQUS for the thin shell finite element $S8R5$. In this case, an imperfection force at the centre of the shell is applied. The paths of the MS model are shown in terms of the unit load Q versus the average out-of-plane displacement of the central zone, evaluated as the arithmetic mean of the displacements of the atoms marked in red in Figure 7. For the shell, the unit load Q versus the out-of-plane displacement of the centre are shown.

In Figure 8, the results of the zigzag and armchair compression tests are shown, for the case of simple support only on the loaded sides. The equilibrium paths are given very far beyond the critical points and,

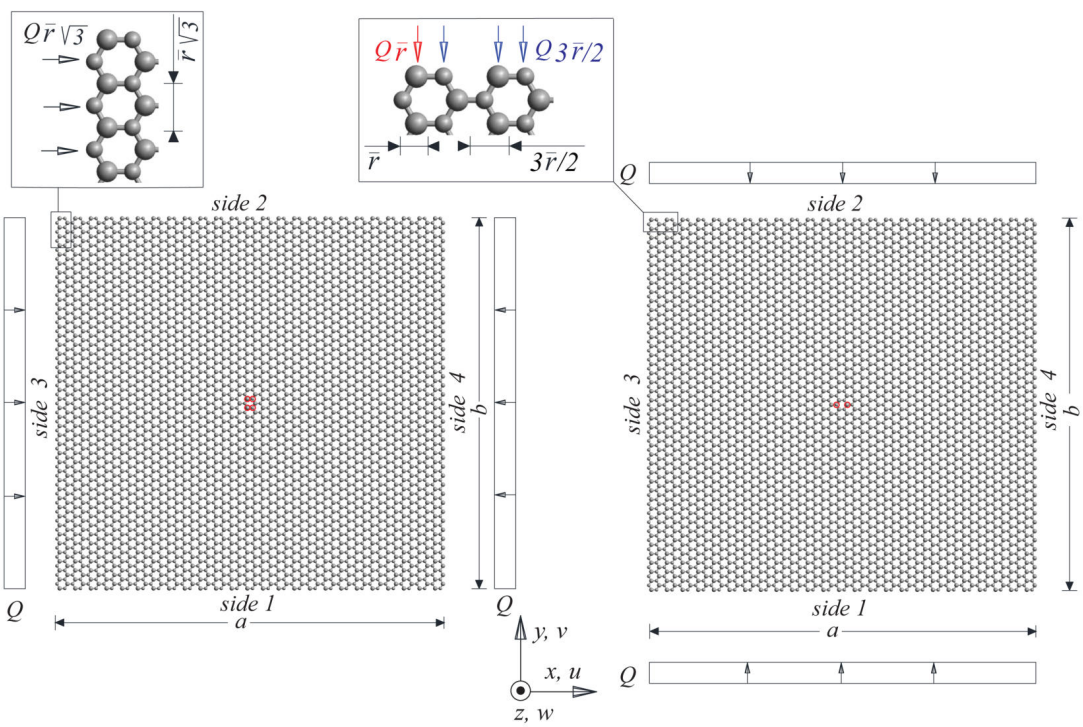

Figure 7. BN sheet under compression loads in the zigzag (left) and armchair (right) directions.

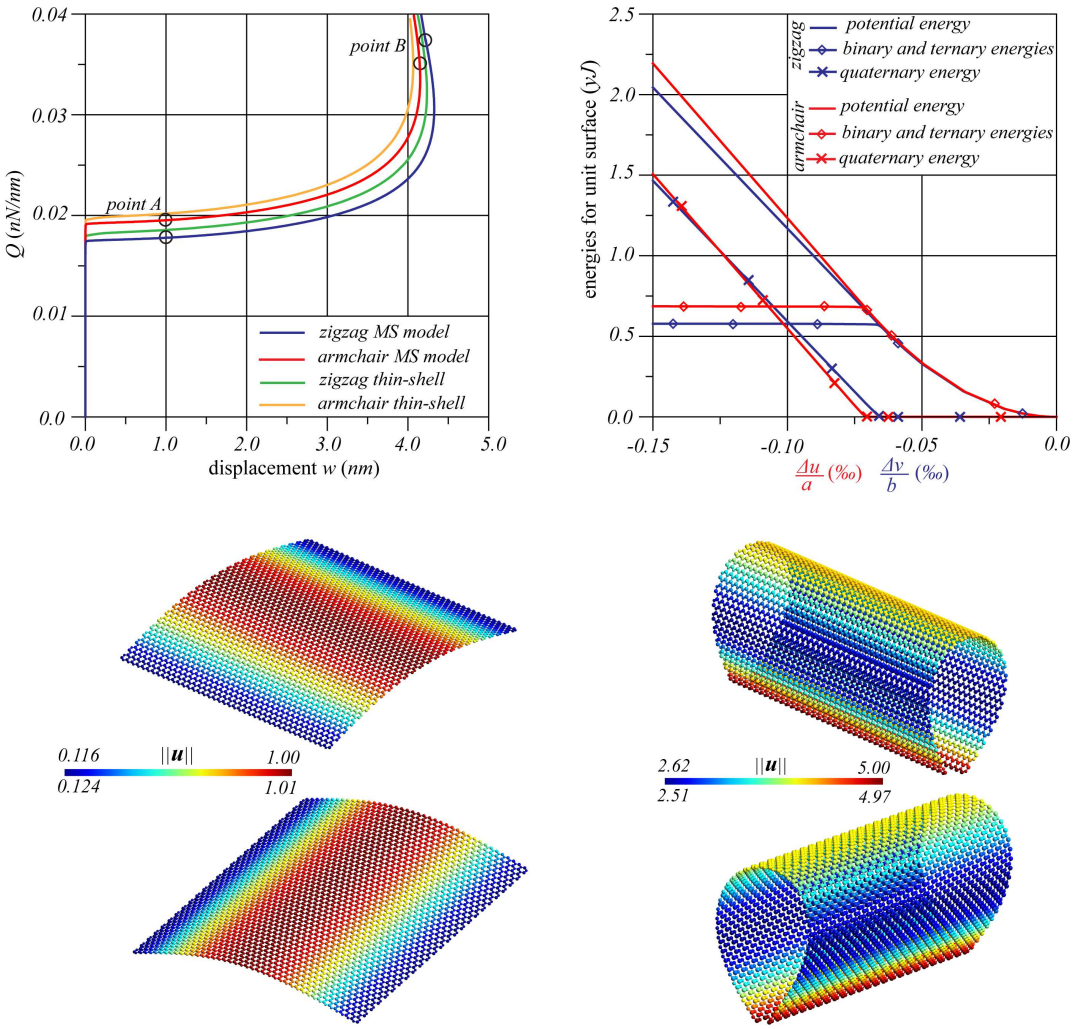

Figure 8. Zigzag and armchair compression tests of a BN sheet, simply supported only on the loaded sides: equilibrium paths (top left), energy trends (top right) and deformed configurations at points A (bottom left) and B (bottom right).

for the MS model some significant configurations are also depicted in Figure 8. For both tests and both models we observe a substantial Euler-like behavior, with a stable postcritical branch (see Figure 8, top left); for the MS model, apart from imperceptible local effects, the deformed configurations at first evoke an half-wave in the direction of the load (see Figure 8, bottom left) and then approach a drop-like shape (see Figure 8, bottom right).

Table 3 shows a comparison between the critical loads Q_{cr} of the MS model, evaluated at the onset of buckling, and their analytical counterpart obtained from the Eulerian theory of thin shells [S. P. Timoshenko and J. M. Gere 1963], namely $Q_E = \pi^2 D/a^2$ for the zigzag test and $Q_E = \pi^2 D/b^2$ for the armchair one.

direction	Eulerian loads, Q_E (nN/nm)	critical loads, Q_{cr} (nN/nm)
zigzag	0.0185	0.0175
armchair	0.0200	0.0191

Table 3. Eulerian loads versus Critical loads for a BN sheet compressed and simply supported on the loaded sides.

The results provide an estimate of the approximation with which the shell model reconstructs the behavior of the atomistic system, at least in relation to critical loads. This approximation is about 6% in the zigzag test and of about 5% in the armchair test. In relation to chirality, the apparently not insignificant effects are mostly due to the fact that the sheet is not perfectly square, being the values of a and b different. Overall, the equilibrium paths provided by the MS and shell models are very similar. This also suggests that the hypothesis of linear elasticity made for the shell does not have a great relevance in these results. And vice versa, it seems to suggest a possible simplification of the interatomic potential in its simplest form of harmonic potential, at least, as far as buckling phenomena are concerned.

In Figure 8 (top right), the trends of the potential energy of the sheet are shown in the range of the equilibrium path corresponding to the precritical phase and to the initial postcritical one. The energy contributions are shown as decoupled, separating the contribution due to membrane deformation, that is, the sum of binary and ternary energies, from the quaternary contribution, which is inherently flexural. All the energies are measured with respect to the resting state of the sheet and given per unit area of the reference surface, while the deformation of the sheet is given in terms of the aforementioned engineering strains ε. Diagrams in Figure 8 show that precritical behavior employs purely membranal energy, while postcritical one uses bending energy. Moreover, it is worth noting that energy is quadratic in the precritical phase.

Figure 9 shows the results of zigzag and armchair compression tests of a BN sheet simply supported on all the sides. The equilibrium paths provided by the MS model and the shell model are shown in the deep postcritical behavior (see Figure 9, left column, top) and, for the MS model, the configurations at the points A, B and C are also pictured (see Figure 9, right column).

The four equilibrium paths are qualitatively quite similar: after a first bifurcation, the initially stable postcritical path has a very high limit point for loads, followed by an unstable branch. The unstable branches are, however, quite different from the quantitative point of view, both in relation to the armchair or zigzag direction of the compression, and in relation to the approximate capacity of the shell model. In fact, in the zigzag test the unstable branch is not well fitted by the shell model.

The configurations at points A, B and C, shown in Figure 9 (right column), reveal a postcritical behavior characterized by the accentuation of the initial half-wave critical mode up to an increasing crumple. It is worth noting that, along the unstable branch of the zigzag test, the deformed configurations are not symmetric; they differ from what happens for the armchair test. Again, these nonsymmetric configurations, not encountered for graphene [Genoese et al. 2019a], can be explained by the presence of B and N atoms in the rings. The nonsymmetric configurations, obviously, are not reproducible by the isotropic shell model and this, in our opinion, is the reason of its loss of accuracy along the unstable branch of the zigzag test. Instead, the linear elasticity of the shell does not significantly affect the results as we can deduce from the almost total overlap of the paths for the armchair test.

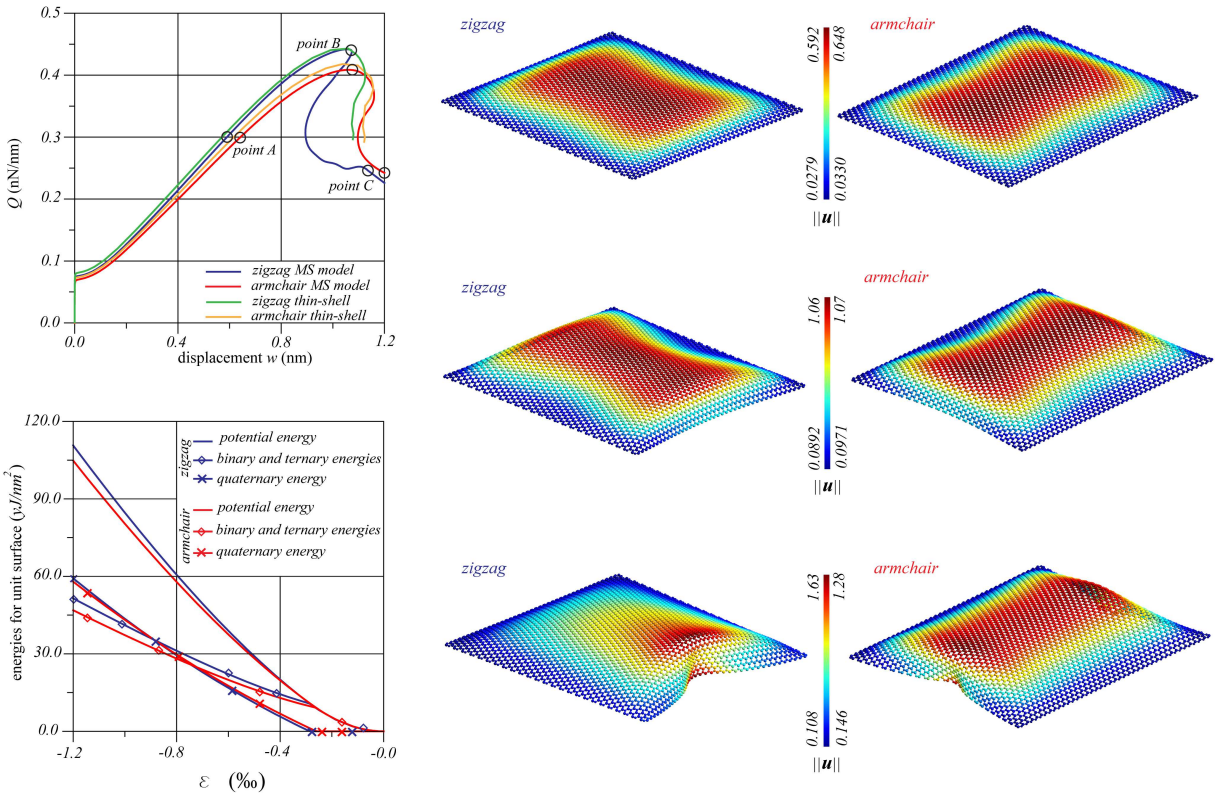

Figure 9. Zigzag and armchair compression tests of a BN sheet, simply supported on all the sides; left column: equilibrium paths (top) and energy trends (bottom); right column: deformed configurations at points A (top), B (middle) and C (bottom).

Once again, a comparison is performed between the critical loads Q_{cr} and the Eulerian ones [S. P. Timoshenko and J. M. Gere 1963], namely $Q_E = k\pi^2 D/b^2$ for the zigzag case and $Q_E = k\pi^2 D/a^2$ for the armchair case, with $k = 4$. The comparison is given in Table 4 from which a percentage distance of about 3% and of about 7% comes to light for the zigzag case and for the armchair case, respectively.

Furthermore, a very low influence of chirality in the critical behavior of the sheet emerges, differently from what is obtained in the advanced postcritical phase. In Figure 9 (left column, bottom), the energy diagrams reveal that the precritical behavior of the sheet is linear and purely membranal, as in the previous examples. However, unlike in the previous examples, membranal and flexural energies coexist in the postcritical behavior.

direction	Eulerian loads, Q_E (nN/nm)	critical loads, Q_{cr} (nN/nm)
zigzag	0.0802	0.0776
armchair	0.0739	0.0694

Table 4. Eulerian loads versus critical loads for a BN sheet compressed and simply supported on all sides.

5.3. ***Shear tests.*** As completion of our numerical investigation, the BN sheet of finite size is studied also under pure shear loads and under shear loads in the zigzag direction and in the armchair direction, as shown in Figure 10. In all the shear tests, conditions of simple support on the out-of-plane displacements are given for all sides. As for the in-plane displacements, case by case, different constraints are assumed. In particular, the pure shear test is performed assuming $\sum_{i=1}^{n_a} u_i = 0$, $\sum_{i=1}^{n_a} v_i = 0$ and $\sum_{i=1}^{n_a} (v_i \tilde{x}_i - u_i \tilde{y}_i) = 0$, where $\tilde{x}_i$ and $\tilde{y}_i$ are the atomic coordinates with respect to the centre of the sheet. The zigzag and armchair shear tests are performed assuming $u_i = v_i = 0$ on side 1 and $v_i = 0$ on side 2, and $u_i = v_i = 0$ on side 3 and $u_i = 0$ on side 4, respectively. Small imperfection forces are given perpendicularly to the plane of the sheet. In particular, only one scenario is considered in the pure shear test, in which forces that are equal to each other are applied to the atoms marked in red.

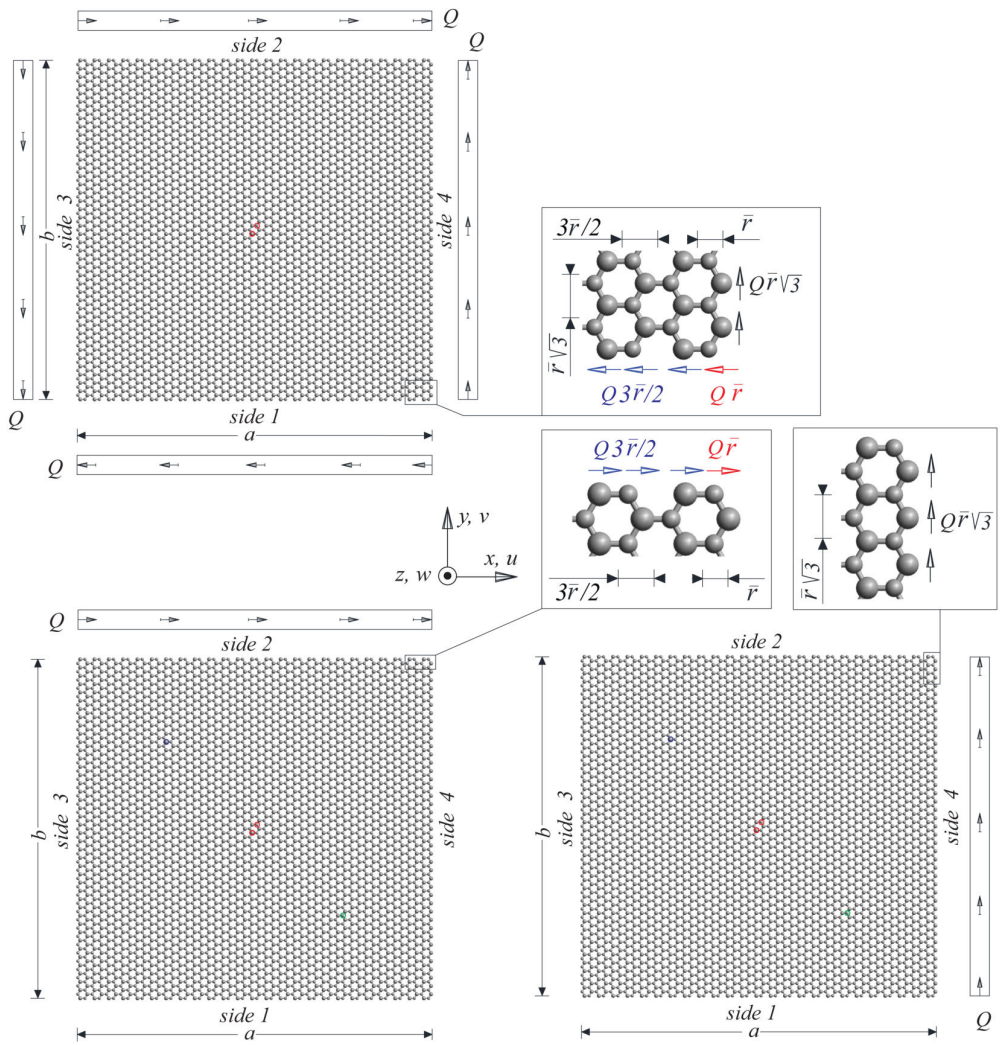

Figure 10. The load settings of the shear tests for the BN sheet: pure shear test (top), zigzag shear test (bottom left) and armchair shear test (bottom right).

In the zigzag and armchair shear tests, two scenarios are instead taken into account: the imperfection scenario 1 consists of a positive force and a negative force on the atoms marked in green and blue, respectively; the imperfection scenario 2 consists of forces equal to each other on the atoms marked in red. These scenarios have been suggested by a preliminary study of the buckling modes of the equivalent shell, which revealed two nearly coincident modes, the first with two bubbles of opposite sign and the second with a single bubble, all elongated in the direction of the principal traction. The equilibrium paths are given in terms of the load Q versus the average out-of-plane displacement of the central zone, evaluated as the arithmetic mean of the displacements of the atoms marked in red in the pure shear test and in the zigzag and armchair shear tests under the imperfection scenario 2, or versus the out-of-plane displacement of the atom marked in green in the zigzag and armchair shear tests under the imperfection scenario 1. Also in this case comparisons with the results of the equivalent shell are performed, with imperfection forces and plotted displacements practically identical to those selected for the atomistic systems.

The results of the pure shear test are shown in Figure 11. The equilibrium paths and some significant deformed configurations obtained through the MS model are given in Figure 11 (left column, top and right column). In the postcritical phase, the equilibrium path (see Figure 11, left column, top) presents two subsequent stable branches and a final unstable branch. The initial postcritical configurations are essentially characterized by a central bubble elongated towards the direction of the principal traction (see Figure 11, right column, top). During the progression of the postcritical phase this bubble is replaced by two bubbles (see Figure 11, right column, middle) to which local distortions add, near the vertices and in the direction of the principal traction, along the unstable branch (see Figure 11, right column, bottom). The shell model instead shows a stable postcritical branch only, which fits well with the first stable branch of the path of the MS model.

The critical load Q_{cr} and the Eulerian one [S. P. Timoshenko and J. M. Gere 1963], that is, $Q_E = k\pi^2 D/b^2$ where $k = 5.35+4(b/a)^2 = 9.0337$, are compared in Table 5. As seen in this table, a percentage distance of about 11% is registered between Q_{cr} and Q_E.

At this point, it is worth highlighting that the postcritical behavior of the shell is again qualitatively similar to those encountered for graphene [Genoese et al. 2019a], which exhibits only a postcritical stable branch, related to configurations with a simple bubble up to a limit point. In the case of BN sheet, the presence of two stable branches seems to be mainly related to the presence of two different atoms; this suggests that the loss of accuracy of the shell model in the deep postcritical phase is due to the lack of small scale effects. Finally in Figure 11 (left column, bottom), the potential energy is given as a function of $\gamma = \Delta u/b + \Delta v/a = (\bar{u}_2 - \bar{u}_1)/b + (\bar{v}_4 - \bar{v}_3)/a$. Similarly to the case of a compressed sheet simply supported on all the sides, we notice a purely membranal and linear precritical behavior, while in the postcritical phase membranal and flexural energies coexist.

Eulerian loads, Q_E (nN/nm)	critical loads, Q_{cr} (nN/nm)
0.181	0.163

Table 5. Eulerian loads versus critical loads for the pure shear test of a BN sheet.

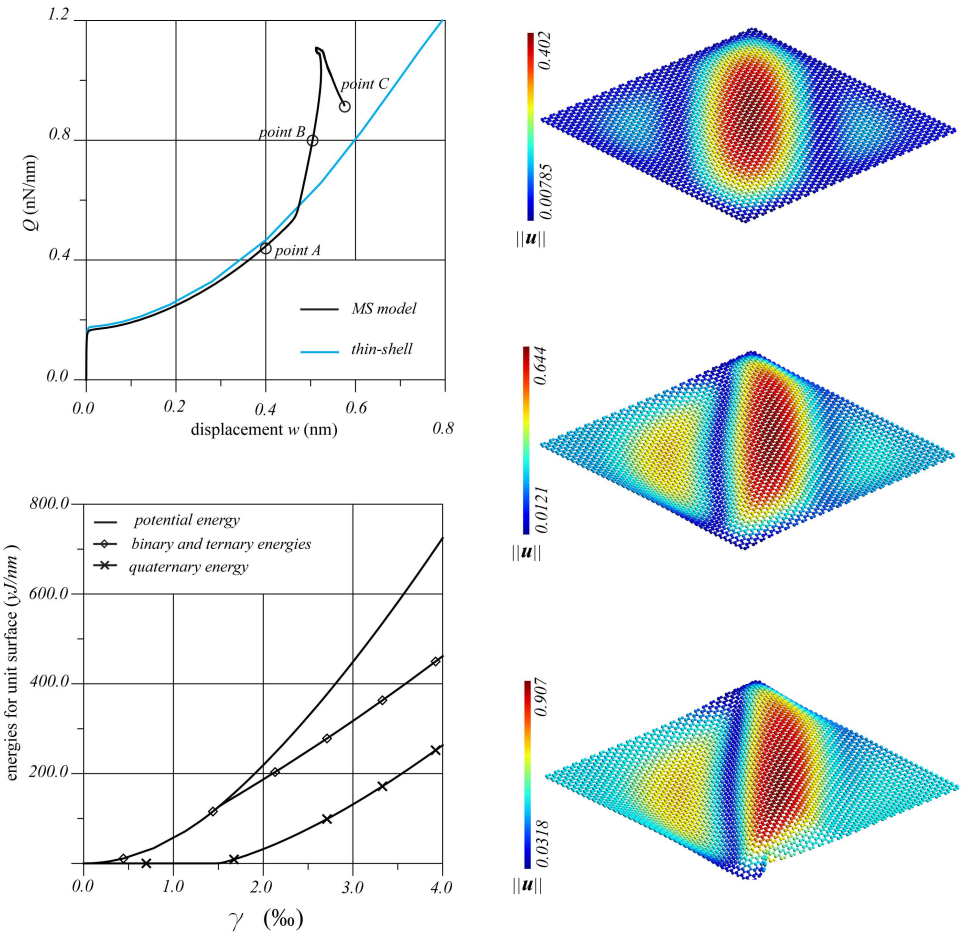

Figure 11. Pure shear test of a BN sheet; left column: equilibrium path (top) and energy trends (bottom); right column: deformed configurations at points A (top), B (middle) and C (bottom).

In figures 12 and 13, the equilibrium paths and some significant deformed configurations of the MS model are given for the zigzag and armchair shear tests under the two imperfection scenarios, corresponding to a two bubbles and a one bubble configurations, respectively. The related critical loads are also listed in Table 6.

direction	imperfection scenario 1	imperfection scenario 2
zigzag	0.149	0.158
armchair	0.146	0.153

Table 6. Critical loads (nN/nm) of the zigzag and armchair shear tests of a BN sheet in two imperfection scenarios.

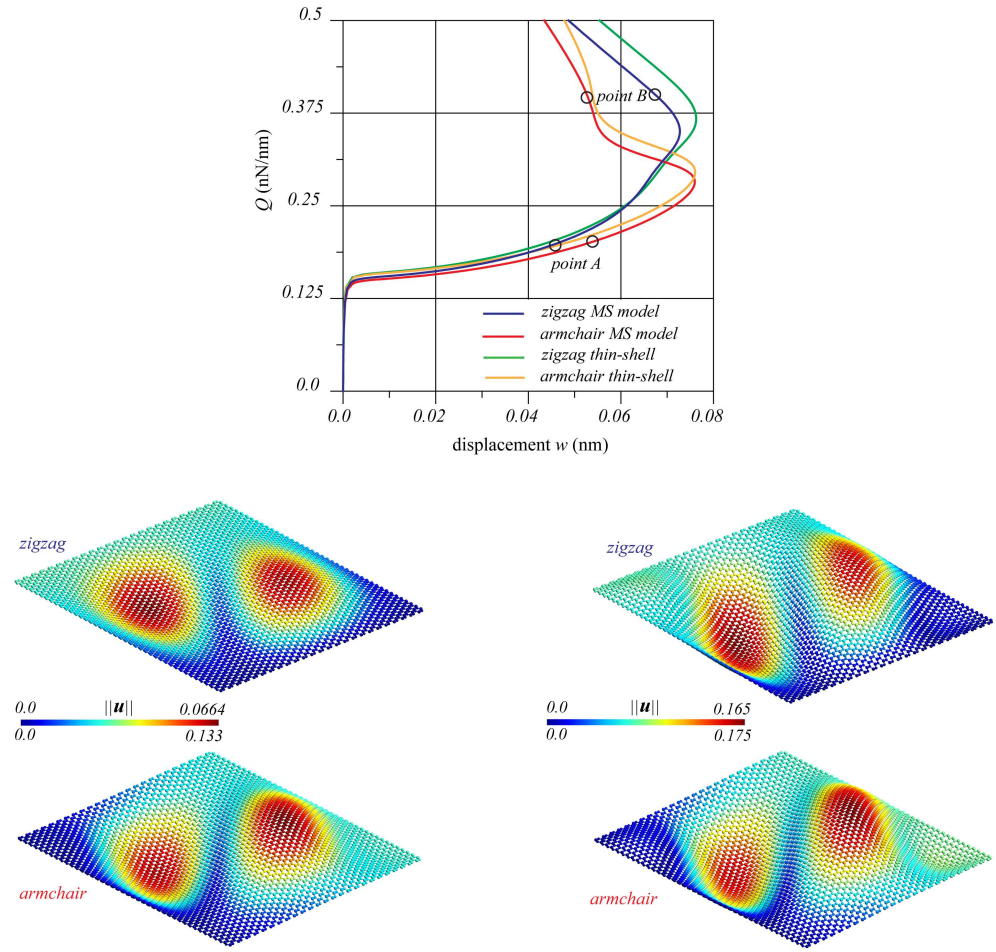

Figure 12. Zigzag and armchair shear tests of a BN sheet under the imperfection scenario 1: equilibrium paths (top) and deformed configurations at points A (bottom left) and B (bottom right).

Results indicate slightly lower loads for the scenario with two bubbles and stable postcritical paths in all the cases, qualitatively well fitted by the shell (see Figure 12, top and Figure 13, top left). With reference to the critical loads we register very small differences, mostly depending on the different values of a and b in the zigzag and in the armchair tests. Also the equilibrium paths are almost indistinguishable nearby the critical point and in the initial postcritical phase, on varying the direction of the shear. In a deep postcritical phase they instead differ enough for the presence of different folds, shifted to each other; this can be explained as an amplified effect of the difference between a and b, since this is seen also by the shell model. As for the configurations, results of the MS model indicate an initial progression of the shape with two bubbles (see Figure 12, bottom left) or with one bubble (see Figure 13, top right), according to the imperfection. For both cases, the progression of the postcritical phase is characterized by the addition of two minor bubbles near the sides, giving configurations with two crests and two

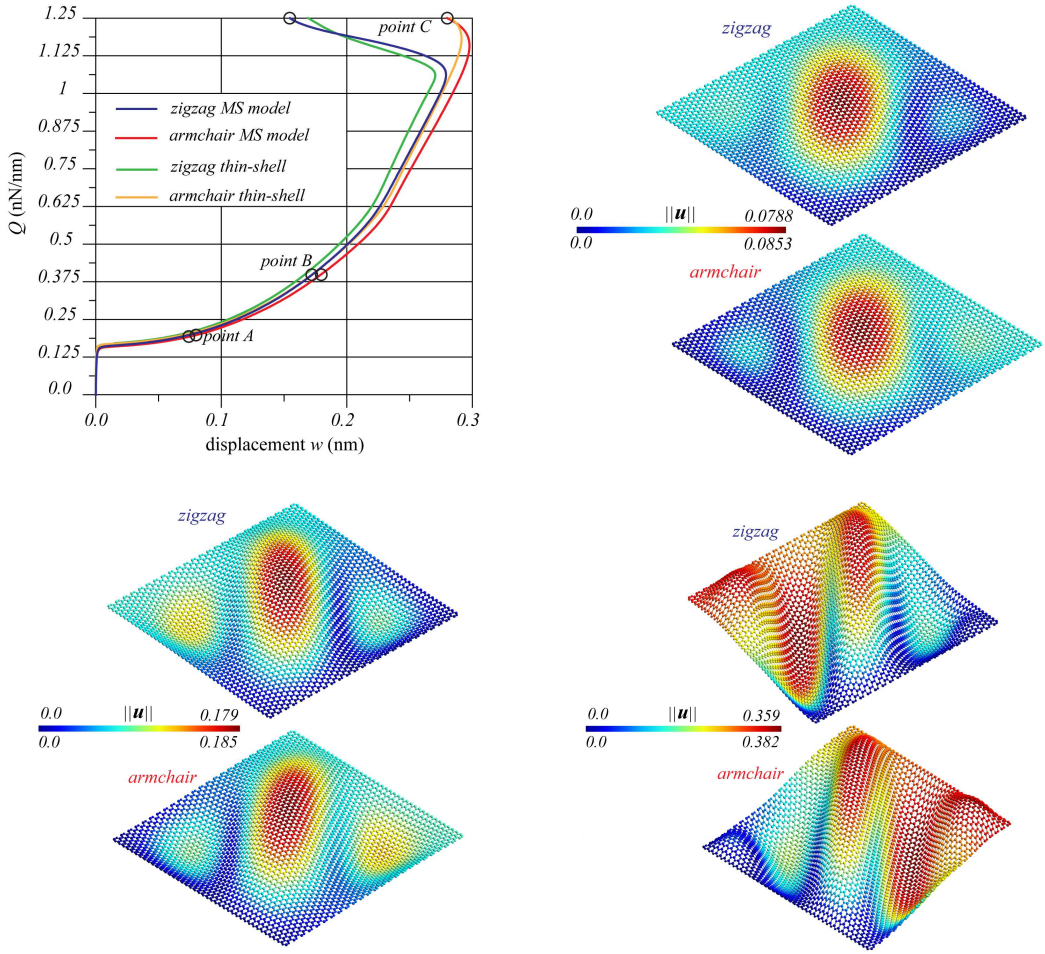

Figure 13. Zigzag and armchair shear tests of a BN sheet under the imperfection scenario 2: equilibrium paths (top left) and deformed configurations at points A (top right), B (bottom left) and C (bottom right).

throats along the direction of the principal compression for the imperfection scenario 1 (see Figure 12, bottom right) or with one crest and two throats along the direction of the principal compression for the imperfection scenario 2 (see Figure 13, bottom left). In the latter case, the configurations with one crest and two thoats are replaced by configurations with more bubbles consisting of three crests and two throats (see Figure 13, bottom right).

6. Conclusion

In this paper, a numerical model for hexagonal BN nanostructures, based on binary, ternary and quaternary interactions, has been presented and a discussion about the choice of the parameters at stake has been carried out. An assessment of the model with respect to the *ab-initio* results in terms of the tensile failure properties of a sheet has been performed, by considering periodic tensile tests in both zigzag and

armchair directions. Once validated, the model has been used to study the response of a BN sheet of finite size under tension, compression and shear in the zigzag and in the armchair directions, and under pure shear. Analysis of results has demonstrated the accuracy of the adopted parameters and has brought to light some features already found in the case of graphene [Genoese et al. 2019a; 2019b]. In more detail, we have observed bifurcation phenomena in all the tests on the sheet of finite size; with regard to buckling in the compression and shear tests, critical and initial postcritical behaviors are well reproduced by a linear elastic thin shell model. Different to the case of graphene, in the tensile tests the behavior of the sheet turned out to be nonsymmetric with respect to the vertical axis, as well as in the compression test in the zigzag direction. This can be explained trough the diatomicity of the sheet.

The model, here presented, can certainly be used to study the mechanical behaviors of other hexagonal BN nanostructures, not deeply investigated in the literature, such as BN nanoribbons or nanotubes.

Appendix A: the derivatives of the potential functions

The derivatives of (2) are

$$\frac{dU_{ij}}{dr_{ij}} = 2\bar{U}\beta\left[1 - e^{-\beta(r_{ij}-\bar{r})}\right]e^{-\beta(r_{ij}-\bar{r})}, \tag{35a}$$

$$\frac{dU_{ijk}}{d\cos\vartheta_{ijk}} = 3A\left(1 - 4\cos^2\vartheta_{ijk}\right), \tag{35b}$$

$$\frac{dU_{ijkl}}{d\varphi_{ijkl}} = V\sin\left[2\left(\varphi_{ijkl} - \bar{\varphi}_{ijkl}\right)\right], \tag{35c}$$

$$\begin{gathered}\frac{d^2U_{ij}}{dr_{ij}^2} = 2\bar{U}\beta^2\left[2e^{-\beta(r_{ij}-\bar{r})} - 1\right]e^{-\beta(r_{ij}-\bar{r})}, \\ \frac{d^2\,U_{ijk}}{d\,cos^2\vartheta_{ijk}} = -24A\cos\vartheta_{ijk}, \qquad \frac{d^2\,U_{ijkl}}{d\,\varphi_{ijkl}^2} = 2V\cos\left[2\left(\varphi_{ijkl} - \bar{\varphi}_{ijkl}\right)\right].\end{gathered} \tag{36}$$

Appendix B: the second variation of the potential

The second variation of the potential U is

$$\delta\dot{U} = \sum_b \delta\boldsymbol{r}_{ij}\cdot\dot{\boldsymbol{s}}_{ij}^r + \sum_a\left(\delta\boldsymbol{r}_{ij}\cdot\dot{\boldsymbol{s}}_{ij}^\vartheta + \delta\boldsymbol{r}_{ik}\cdot\dot{\boldsymbol{s}}_{ik}^\vartheta\right) + \sum_d\left(\delta\boldsymbol{r}_{ij}\cdot\dot{\boldsymbol{s}}_{ij}^\varphi + \delta\boldsymbol{r}_{ik}\cdot\dot{\boldsymbol{s}}_{ik}^\varphi + \delta\boldsymbol{r}_{jl}\cdot\dot{\boldsymbol{s}}_{jl}^\varphi\right), \tag{37}$$

where $\dot{\boldsymbol{s}}_{ij}^r$, $\dot{\boldsymbol{s}}_\alpha^\vartheta$, and $\dot{\boldsymbol{s}}_\beta^\varphi$, $\alpha \in \{ij, ik\}$ and $\beta \in \{ij, ik, jl\}$ are the incremental forces related to the various interactions, obtained by variation of (21). In detail, by variation of (21a), one obtains

$$\dot{\boldsymbol{s}}_{ij}^r = \frac{d^2U_{ij}}{dr_{ij}^2}\tilde{\boldsymbol{r}}_{ij}\dot{r}_{ij} + \frac{dU_{ij}}{dr_{ij}}\dot{\tilde{\boldsymbol{r}}}_{ij}. \tag{38a}$$

Furthermore, evaluating $\dot{r}_{ij}$ and $\dot{\tilde{\boldsymbol{r}}}_{ij}$ according to (7) and (8), one obtains

$$\dot{\boldsymbol{s}}_{ij}^r = \left[\left(\frac{d^2U_{ij}}{dr_{ij}^2} - \frac{1}{r_{ij}}\frac{dU_{ij}}{dr_{ij}}\right)\tilde{\boldsymbol{r}}_{ij}\otimes\tilde{\boldsymbol{r}}_{ij} + \frac{1}{r_{ij}}\frac{dU_{ij}}{dr_{ij}}\boldsymbol{I}\right]\dot{\boldsymbol{r}}_{ij}. \tag{38b}$$

Similarly, by variation of (21b), one obtains

$$\dot{\boldsymbol{s}}^{\vartheta}_{\alpha} = \frac{d^2 U_{ijk}}{d\cos^2\vartheta_{ijk}}\boldsymbol{n}^{\vartheta}_{\alpha}\dot{\cos}\vartheta_{ijk} + \frac{dU_{ijk}}{d\cos\vartheta_{ijk}}\dot{\boldsymbol{n}}^{\vartheta}_{\alpha}, \quad \alpha \in \{ij, ik\}. \tag{39a}$$

By recalling (10), we also obtain

$$\boldsymbol{n}^{\vartheta}_{\alpha}\dot{\cos}\vartheta_{ijk} = \left(\boldsymbol{n}^{\vartheta}_{\alpha}\otimes\boldsymbol{n}^{\vartheta}_{ij}\right)\dot{\boldsymbol{r}}_{ij} + \left(\boldsymbol{n}^{\vartheta}_{\alpha}\otimes\boldsymbol{n}^{\vartheta}_{ik}\right)\dot{\boldsymbol{r}}_{ik}. \tag{39b}$$

The second term in (39a) requires the calculation of $\dot{\boldsymbol{n}}^{\vartheta}_{\alpha}$, $\alpha \in \{ij, ik\}$. From (11), it follows that

$$\begin{aligned}\dot{\boldsymbol{n}}^{\vartheta}_{ij} &= \left(\frac{\dot{1}}{r_{ij}}\right)(\tilde{\boldsymbol{r}}_{ik} - \cos\vartheta_{ijk}\tilde{\boldsymbol{r}}_{ij}) + \frac{1}{r_{ij}}\dot{\tilde{\boldsymbol{r}}}_{ik} - \frac{1}{r_{ij}}\tilde{\boldsymbol{r}}_{ij}\dot{\cos}\vartheta_{ijk} - \frac{\cos\vartheta_{ijk}}{r_{ij}}\dot{\tilde{\boldsymbol{r}}}_{ij}\\ &= -\frac{1}{r_{ij}}\left[\boldsymbol{n}^{\vartheta}_{ij}\otimes\tilde{\boldsymbol{r}}_{ij} + \tilde{\boldsymbol{r}}_{ij}\otimes\boldsymbol{n}^{\vartheta}_{ij} + \frac{\cos\vartheta_{ijk}}{r_{ij}}(\boldsymbol{I} - \tilde{\boldsymbol{r}}_{ij}\otimes\tilde{\boldsymbol{r}}_{ij})\right]\dot{\boldsymbol{r}}_{ij}\\ &\quad + \frac{1}{r_{ij}}\left[\frac{1}{r_{ik}}(\boldsymbol{I} - \tilde{\boldsymbol{r}}_{ik}\otimes\tilde{\boldsymbol{r}}_{ik}) - \tilde{\boldsymbol{r}}_{ij}\otimes\boldsymbol{n}^{\vartheta}_{ik}\right]\dot{\boldsymbol{r}}_{ik},\end{aligned} \tag{39c}$$

and likewise

$$\dot{\boldsymbol{n}}^{\vartheta}_{ik} = \frac{1}{r_{ik}}\left[\frac{1}{r_{ij}}(\boldsymbol{I} - \tilde{\boldsymbol{r}}_{ij}\otimes\tilde{\boldsymbol{r}}_{ij}) - \tilde{\boldsymbol{r}}_{ik}\otimes\boldsymbol{n}^{\vartheta}_{ij}\right]\dot{\boldsymbol{r}}_{ij} - \frac{1}{r_{ik}}\left[\boldsymbol{n}^{\vartheta}_{ik}\otimes\tilde{\boldsymbol{r}}_{ik} + \tilde{\boldsymbol{r}}_{ik}\otimes\boldsymbol{n}^{\vartheta}_{ik} + \frac{\cos\vartheta_{ijk}}{r_{ik}}(\boldsymbol{I} - \tilde{\boldsymbol{r}}_{ik}\otimes\tilde{\boldsymbol{r}}_{ik})\right]\dot{\boldsymbol{r}}_{ik}. \tag{39d}$$

So, similarly, by variation of (21c), we obtain

$$\dot{\boldsymbol{s}}^{\varphi}_{\beta} = \frac{d^2 U_{ijkl}}{d\varphi^2_{ijkl}}\boldsymbol{n}^{\varphi}_{\beta}\dot{\varphi}_{ijkl} + \frac{dU_{ijkl}}{d\varphi_{ijkl}}\dot{\boldsymbol{n}}^{\varphi}_{\beta}, \quad \beta \in \{ij, ik, jl\}. \tag{40a}$$

In light of Eq. (17), we also have

$$\boldsymbol{n}^{\varphi}_{\beta}\dot{\varphi}_{ijkl} = (\boldsymbol{n}^{\varphi}_{\beta}\otimes\boldsymbol{n}^{\varphi}_{ij})\,\dot{\boldsymbol{r}}_{ij} + (\boldsymbol{n}^{\varphi}_{\beta}\otimes\boldsymbol{n}^{\varphi}_{ik})\,\dot{\boldsymbol{r}}_{ik} + (\boldsymbol{n}^{\varphi}_{\beta}\otimes\boldsymbol{n}^{\varphi}_{jl})\,\dot{\boldsymbol{r}}_{jl}. \tag{40b}$$

To complete (40a), we calculate $\dot{\boldsymbol{n}}^{\varphi}_{\beta}$, $\beta \in \{ij, ik, jl\}$. From (18), one obtains

$$\begin{aligned}\dot{\boldsymbol{n}}^{\varphi}_{ij} = &-\frac{1}{r^2_{ij}}\left(\cos\vartheta_{ijk}\,\boldsymbol{N}_{ijk}\,\tilde{\boldsymbol{r}}^{*}_{ik} + \cos\vartheta_{jil}\,\boldsymbol{N}_{jil}\,\tilde{\boldsymbol{r}}^{*}_{jl} + \boldsymbol{n}^{\varphi}_{ij}\otimes\boldsymbol{r}_{ij} + \boldsymbol{n}^{\varphi}_{ik}\otimes\boldsymbol{r}_{ik} + \boldsymbol{n}^{\varphi}_{jl}\otimes\boldsymbol{r}_{jl}\right)\dot{\boldsymbol{r}}_{ij}\\ &+\frac{1}{r_{ij}\,r_{ik}}\left(\cos\vartheta_{ijk}\,\boldsymbol{N}_{ijk}\,\tilde{\boldsymbol{r}}^{*}_{ij} - \frac{1}{n_{ijk}}\tilde{\boldsymbol{n}}_{ijk}\otimes\tilde{\boldsymbol{r}}_{ij}\right)\dot{\boldsymbol{r}}_{ik}\\ &+\frac{1}{r_{ij}\,r_{jl}}\left(\cos\vartheta_{jil}\,\boldsymbol{N}_{jil}\,\tilde{\boldsymbol{r}}^{*}_{ij} - \frac{1}{n_{jil}}\tilde{\boldsymbol{n}}_{jil}\otimes\tilde{\boldsymbol{r}}_{ij}\right)\dot{\boldsymbol{r}}_{jl},\end{aligned} \tag{40c}$$

$$\dot{\boldsymbol{n}}^{\varphi}_{ik} = \frac{1}{r_{ij}\,r_{ik}}\left(\boldsymbol{N}_{ijk}\,\tilde{\boldsymbol{r}}^{*}_{ik} + \frac{1}{n_{ijk}}\tilde{\boldsymbol{n}}_{ijk}\otimes\tilde{\boldsymbol{r}}_{ij}\right)\dot{\boldsymbol{r}}_{ij} - \frac{1}{r^2_{ik}}\boldsymbol{N}_{ijk}\,\tilde{\boldsymbol{r}}^{*}_{ij}\,\dot{\boldsymbol{r}}_{ik}, \tag{40d}$$

$$\dot{\boldsymbol{n}}^{\varphi}_{jl} = \frac{1}{r_{ij}\,r_{jl}}\left(\frac{1}{n_{jil}}\tilde{\boldsymbol{n}}_{jil}\otimes\tilde{\boldsymbol{r}}_{ij} - \boldsymbol{N}_{jil}\,\tilde{\boldsymbol{r}}^{*}_{jl}\right)\dot{\boldsymbol{r}}_{ij} + \frac{1}{r^2_{jl}}\boldsymbol{N}_{jil}\,\tilde{\boldsymbol{r}}^{*}_{ij}\,\dot{\boldsymbol{r}}_{jl}, \tag{40e}$$

where $\boldsymbol{N}_{\gamma} = \frac{1}{n^2_{\gamma}}(2\tilde{\boldsymbol{n}}_{\gamma}\otimes\tilde{\boldsymbol{n}}_{\gamma} - \boldsymbol{I})$, with $\gamma \in \{ijk, jil\}$ and where $\boldsymbol{a}^{*}$ is the skew-symmetric tensor isomorphic to the vector $\boldsymbol{a}$.

The expressions (39c) and (39d) of $\dot{\boldsymbol{n}}_{ij}^{\vartheta}$ and $\dot{\boldsymbol{n}}_{ik}^{\vartheta}$ and the expressions (40c)–(40e) of $\dot{\boldsymbol{n}}_{ij}^{\varphi}$, $\dot{\boldsymbol{n}}_{ik}^{\varphi}$ and $\dot{\boldsymbol{n}}_{jl}^{\varphi}$ are compact, but they do not make visible, as they stand, the symmetry of the tangent operator, given that it derives from the second variation of the potential U. To view this symmetry, equations (39c) and (39d) need to be manipulated using (11). As for the manipulation of (40c)–(40e), the interested reader is referred to [Blondel and Karplus 1996].

Acknowledgements

We are very grateful to the University "Roma Tre" for cofunding the research contract of PhD Alessandra Genoese and to the Italian Ministry of University, Research and Education for cofunding the research contract of PhD Andrea Genoese.

References

[Akinwande et al. 2017] D. Akinwande, C. J. Brennan, J. S. Bunch, P. Egberts, J. R. Felts, H. Gao, R. Huang, J.-S. Kim, T. Li, Y. Li, K. M. Liechti, N. Lu, H. S. Park, E. J. Reed, P. Wang, B. I. Yakobson, T. Zhang, Y.-W. Zhang, Y. Zhou, and Y. Zhu, "A review on mechanics and mechanical properties of 2D materials — graphene and beyond", *Extreme Mech. Lett.* **13** (2017), 42–77.

[Auffray et al. 2015] N. Auffray, J. Dirrenberger, and G. Rosi, "A complete description of bi-dimensional anisotropic strain-gradient elasticity", *Int. J. Solids Struct.* **69-70** (2015), 195–206.

[Blondel and Karplus 1996] A. Blondel and M. Karplus, "New formulation for derivatives of torsion angles and improper torsion angles in molecular mechanics: elimination of singularities", *J. Comput. Chem.* **17**:9 (1996), 1132–1141.

[Casady and Johnson 1996] J. B. Casady and R. W. Johnson, "Status of silicon carbide (SiC) as a wide-bandgap semiconductor for high temperature applications: a review", *Solid State Electron.* **39**:10 (1996), 1409–1422.

[Şahin et al. 2009] H. Şahin, S. Cahangirov, M. Topsakal, E. Bekaroglu, E. Akturk, R. T. Senger, and S. Ciraci, "Monolayer honeycomb structures of group-IV elements and III-V binary compounds: first-principles calculations", *Phys. Rev. B* **80**:15 (2009), 155453.

[Davini et al. 2017] C. Davini, A. Favata, and R. Paroni, "A new material property of graphene: the bending Poisson coefficient", *EPL* **118**:2 (2017), 26001. arXiv

[Favata et al. 2014] A. Favata, A. Micheletti, and P. Podio-Guidugli, "A nonlinear theory of prestressed elastic stick-and-spring structures", *Int. J. Eng. Sci.* **80** (2014), 4–20. arXiv

[Fazelzadeh and Ghavanloo 2014] S. A. Fazelzadeh and E. Ghavanloo, "Vibration analysis of curved graphene ribbons based on an elastic shell model", *Mech. Res. Commun.* **56** (2014), 61–68.

[Garcea et al. 1998] G. Garcea, G. A. Trunfio, and R. Casciaro, "Mixed formulation and locking in path-following nonlinear analysis", *Comput. Methods Appl. Mech. Eng.* **165**:1-4 (1998), 247–272.

[Genoese et al. 2017] A. Genoese, A. Genoese, N. L. Rizzi, and G. Salerno, "On the derivation of the elastic properties of lattice nanostructures: the case of graphene sheets", *Compos. B Eng.* **115** (2017), 316–329.

[Genoese et al. 2018a] A. Genoese, A. Genoese, N. L. Rizzi, and G. Salerno, "Force constants of BN, SiC, AlN and GaN sheets through discrete homogenization", *Meccanica* (*Milano*) **53** (2018), 593–611.

[Genoese et al. 2018b] A. Genoese, A. Genoese, and G. Salerno, "Elastic constants of achiral single-wall CNTs: analytical expressions and a focus on size and small scale effects", *Compos. B Eng.* **147** (2018), 207–226.

[Genoese et al. 2019a] A. Genoese, A. Genoese, N. L. Rizzi, and G. Salerno, "Buckling analysis of single-layer graphene sheets using molecular mechanics", *Front. Mater.* **6** (2019), 26.

[Genoese et al. 2019b] A. Genoese, A. Genoese, N. L. Rizzi, and G. Salerno, "On the in-plane failure and post-failure behaviour of pristine and perforated single-layer graphene sheets", *Math. Mech. Solids* **24** (2019), 3418–3443.

[Genoese et al. 2019c] A. Genoese, A. Genoese, and G. Salerno, "On the nanoscale behaviour of single-wall C, BN and SiC nanotubes", *Acta Mech.* **230** (2019), 1105–1128.

[Genoese et al. 2020] A. Genoese, A. Genoese, and G. Salerno, "Buckling and post-buckling analysis of single wall carbon nanotubes using molecular mechanics", *Appl. Math. Model.* (online publication March 2020).

[Ghaffari et al. 2018] R. Ghaffari, T. X. Duong, and R. A. Sauer, "A new shell formulation for graphene structures based on existing ab-initio data", *Int. J. Solids Struct.* **135** (2018), 37–60. arXiv

[Giannopoulos et al. 2016] G. I. Giannopoulos, D.-P. N. Kontoni, and S. K. Georgantzinos, "Efficient FEM simulation of static and free vibration behavior of single walled boron nitride nanotubes", *Superlatt. Microstruct.* **96** (2016), 111–120.

[Glaesener et al. 2019] R. N. Glaesener, C. Lestringant, B. Telgen, and D. M. Kochmann, "Continuum models for stretching- and bending-dominated periodic trusses undergoing finite deformations", *Int. J. Solids Struct.* **171** (2019), 117–134.

[Golberg et al. 2010] D. Golberg, Y. Bando, Y. Huang, T. Terao, M. Mitome, C. Tang, and C. Zhi, "Boron nitride nanotubes and nanosheets", *ACS Nano* **4**:6 (2010), 2979–2993.

[Hollerer 2014] S. Hollerer, "Numerical validation of a concurrent atomistic-continuum multiscale method and its application to the buckling analysis of carbon nanotubes", *Comput. Methods Appl. Mech. Eng.* **270** (2014), 220–246.

[Jiang and Guo 2011] L. Jiang and W. Guo, "A molecular mechanics study on size-dependent elastic properties of single-walled boron nitride nanotubes", *J. Mech. Phys. Solids* **59**:6 (2011), 1204–1213.

[Korobeynikov et al. 2015] S. N. Korobeynikov, V. V. Alyokhin, B. D. Annin, and A. V. Babichev, "Quasi-static buckling simulation of single-layer graphene sheets by the molecular mechanics method", *Math. Mech. Solids* **20**:7 (2015), 836–870.

[Korobeynikov et al. 2018] S. N. Korobeynikov, V. Alyokhin, and A. V. Babichev, "Simulation of mechanical parameters of graphene using the DREIDING force field", *Acta Mech.* **229** (2018), 2343–2378.

[Krishnan et al. 1998] A. Krishnan, E. Dujardin, T. W. Ebbesen, P. N. Yianilos, and M. M. J. Treacy, "Young's modulus of single-walled nanotubes", *Phys. Rev. B* **58** (1998), 14013–14019.

[Kudin et al. 2001] K. N. Kudin, G. E. Scuseria, and B. I. Yakobson, "C_2F, BN, and C nanoshell elasticity from *ab initio* computations", *Phys. Rev. B* **64**:23 (2001), 235406.

[Kumar et al. 2018] R. Kumar, R. Singh, D. Hui, L. Feo, and F. Fraternali, "Graphene as biomedical sensing element: state of art review and potential engineering applications", *Compos. B Eng.* **134** (2018), 193–206.

[Le and Nguyen 2015] M.-Q. Le and D.-T. Nguyen, "Determination of elastic properties of hexagonal sheets by atomistic finite element method", *J. Comput. Theor. Nanosci.* **12**:4 (2015), 566–574.

[Mayo et al. 1990] S. L. Mayo, B. D. Olafson, and W. A. Goddard III, "DREIDING: a generic force field for molecular simulations", *J. Phys. Chem.* **94**:26 (1990), 8897–8909.

[Mohan et al. 2018] V. B. Mohan, K.-T. Lau, D. Hui, and D. Bhattacharyya, "Graphene-based materials and their composites: a review on production, applications and product limitations", *Compos. B Eng.* **142** (2018), 200–220.

[Mpourmpakis et al. 2006] G. Mpourmpakis, G. E. Froudakis, G. P. Lithoxoos, and J. Samios, "SiC nanotubes: a novel material for hydrogen storage", *Nano Lett.* **6**:8 (2006), 1581–1583.

[Nguyen and Nguyen 2016] B. H. Nguyen and V. H. Nguyen, "Promising applications of graphene and graphene-based nanostructures", *Nanosci. Nanotechnol.* **7**:2 (2016), 023002.

[Nozaki and Itoh 1996] H. Nozaki and S. Itoh, "Structural stability of BC_2N", *J. Phys. Chem. Solids* **57**:1 (1996), 41–49.

[Ouyang et al. 2010] T. Ouyang, Y. Chen, Y. Xie, K. Yang, Z. Bao, and J. Zhong, "Thermal transport in hexagonal boron nitride nanoribbons", *Nanotechnology* **21**:24 (2010), 245701.

[Rappé et al. 1992] A. K. Rappé, C. J. Casewit, K. S. Colwell, W. A. Goddard III, and W. M. Skiff, "UFF, a full periodic table force field for molecular mechanics and molecular dynamics simulations", *J. Am. Chem. Soc.* **114**:25 (1992), 10024–10035.

[Riks 1979] E. Riks, "An incremental approach to the solution of snapping and buckling problems", *Int. J. Solids Struct.* **15**:7 (1979), 529–551.

[Rizzi et al. 2019a] G. Rizzi, F. D. Corso, D. Veber, and D. Bigoni, "Identification of second-gradient elastic materials from planar hexagonal lattices. Part I: analytical derivation of equivalent constitutive tensors", *Int. J. Solids Struct.* **176-177** (2019), 1–18.

[Rizzi et al. 2019b] G. Rizzi, F. D. Corso, D. Veber, and D. Bigoni, "Identification of second-gradient elastic materials from planar hexagonal lattices. Part II: mechanical characteristics and model validation", *Int. J. Solids Struct.* **176-177** (2019), 19–35.

[S. P. Timoshenko and J. M. Gere 1963] S. P. Timoshenko and J. M. Gere, *Theory of elastic stability*, McGraw–Hill, 1963.

[Salerno and de Felice 2009] G. Salerno and G. de Felice, "Continuum modeling of periodic brickwork", *Int. J. Solids Struct.* **46**:5 (2009), 1251–1267.

[Sgouros et al. 2018] A. P. Sgouros, G. Kalosakas, K. Papagelis, and C. Galiotis, "Compressive response and buckling of graphene nanoribbons", *Sci. Rep.* **8** (2018), 9593.

[Shima 2012] H. Shima, "Buckling of carbon nanotubes: a state of art review", *Materials* **5**:1 (2012), 47–84. arXiv

[Tserpes and Vatistas 2015] K. I. Tserpes and I. Vatistas, "Buckling analysis of pristine and defected graphene", *Mech. Res. Commun.* **64** (2015), 50–56.

[Tsiamaki et al. 2018] A. S. Tsiamaki, D. E. Katsareas, and N. K. Anifantis, "Influence of temperature on the modal behavior of monolayer graphene sheets", *J. Appl. Phys.* **123**:20 (2018), 204307.

[Vijayaraghavan and Zhang 2018] V. Vijayaraghavan and Z. Zhang, "Effective mechanical properties and thickness determination of boron nitride nanosheets using molecular dynamics simulation", *Nanomaterials* **8**:7 (2018), 546.

[Wu et al. 2013] J. Wu, B. Wang, Y. Wei, R. Yang, and M. Dresselhaus, "Mechanics and mechanically tunable band gap in single-layer hexagonal boron-nitride", *Mater. Res. Lett.* **1**:4 (2013), 200–206.

Received 10 Dec 2019. Revised 17 Feb 2020. Accepted 24 Feb 2020.

ALESSANDRA GENOESE: alessandrag_83@hotmail.it
LIMES, Dipartimento di Architettura, Università Roma Tre, 00184 Rome, Italy

ANDREA GENOESE: andreagenoese_83@hotmail.it
LIMES, Dipartimento di Architettura, Università Roma Tre, 00184 Rome, Italy

GINEVRA SALERNO: ginevra.salerno@uniroma3.it
LIMES, Dipartimento di Architettura, Università Roma Tre, 00184 Rome, Italy

JOURNAL OF MECHANICS OF MATERIALS AND STRUCTURES

msp.org/jomms

Founded by Charles R. Steele and Marie-Louise Steele

EDITORIAL BOARD

ADAIR R. AGUIAR	University of São Paulo at São Carlos, Brazil
KATIA BERTOLDI	Harvard University, USA
DAVIDE BIGONI	University of Trento, Italy
MAENGHYO CHO	Seoul National University, Korea
HUILING DUAN	Beijing University
YIBIN FU	Keele University, UK
IWONA JASIUK	University of Illinois at Urbana-Champaign, USA
DENNIS KOCHMANN	ETH Zurich
MITSUTOSHI KURODA	Yamagata University, Japan
CHEE W. LIM	City University of Hong Kong
ZISHUN LIU	Xi'an Jiaotong University, China
THOMAS J. PENCE	Michigan State University, USA
GIANNI ROYER-CARFAGNI	Università degli studi di Parma, Italy
DAVID STEIGMANN	University of California at Berkeley, USA
PAUL STEINMANN	Friedrich-Alexander-Universität Erlangen-Nürnberg, Germany
KENJIRO TERADA	Tohoku University, Japan

ADVISORY BOARD

J. P. CARTER	University of Sydney, Australia
D. H. HODGES	Georgia Institute of Technology, USA
J. HUTCHINSON	Harvard University, USA
D. PAMPLONA	Universidade Católica do Rio de Janeiro, Brazil
M. B. RUBIN	Technion, Haifa, Israel

PRODUCTION production@msp.org

SILVIO LEVY Scientific Editor

Cover photo: Mando Gomez, www.mandolux.com

See msp.org/jomms for submission guidelines.

JoMMS (ISSN 1559-3959) at Mathematical Sciences Publishers, 798 Evans Hall #6840, c/o University of California, Berkeley, CA 94720-3840, is published in 10 issues a year. The subscription price for 2020 is US $660/year for the electronic version, and $830/year (+$60, if shipping outside the US) for print and electronic. Subscriptions, requests for back issues, and changes of address should be sent to MSP.

JoMMS peer-review and production is managed by EditFLOW® from Mathematical Sciences Publishers.

PUBLISHED BY

mathematical sciences publishers

nonprofit scientific publishing

http://msp.org/

© 2020 Mathematical Sciences Publishers

Journal of Mechanics of Materials and Structures

Volume 15, No. 2 March 2020